

Second Order Defeaturing Error Estimator of Porosity on Structural Elastic Performance in Manufactured Metallic Components

Shiguang Deng^{a,*}, Carl Soderhjelm^a, Diran Apelian^a, Krishnan Suresh^b

^a ACRC, Materials Science and Engineering, University of California, Irvine, CA, USA

^b Mechanical Engineering, University of Wisconsin, Madison, WI, USA

Abstract

Manufactured metallic components often contain non-uniformly distributed pores of complex morphologies. Since such porosity defects have significant influence on material behaviors and affect the usage in high-performance applications, it is significant to understand the impact of porosity characteristics on the behaviors of components. In this work, a gradient-enhanced porosity defeaturing estimator, which allows for the modeling of pore geometry and spatial distribution, is proposed within a general elastostatic framework. In this approach, the first order shape sensitivity is implemented to account for the change in elastic quantity of interests with respect to variations of pore sizes and shapes, which is then supplemented by a second order shape sensitivity whose mixed partial derivative quantifies the interactions between pores in proximity. The efficacy of the proposed method comes from its posterior manner that it only relies on field solutions of reference models where pores are suppressed. In this context, meshing difficulty and solution convergence issue are avoided, which would otherwise arise in a direct finite element analysis on porous structures. The impact of porosity on structural elastic performance is approximated using a second order Taylor expansion where the topological difference between the porous and reference domains is estimated by topological sensitivity; the field variables on pore boundaries are approximated as explicit functions of design variables using exterior formulations. Numerical results show that the elastic performances of components are influenced by the existence of pores. The pore-to-pore interactions are significant when pores are close by.

Keywords: Manufacturing-induced porosity, pore-to-pore interactions, defeaturing, tomography reconstruction, design sensitivity.

1. INTRODUCTION

Porosity is a common process induced defect in many metallic components manufactured using different technologies such as high pressure die casting (HPDC) [1] and direct laser melting (DLM) [2]. In HPDC process, porosity can be formed both as macro-porosity where air is rejected from molten metal and entrapped in the mold as spherical gas bubbles, and/or as micro-shrinkage which occurs in regions with inadequate liquid metal flow [3–5]. On the other hand, the generation of irregularly shaped pores in DLM is a process induced phenomenon which strongly depends on various parameters such as inadequate fusion, incomplete remelting, low powder packing density, and mismatch of powder morphologies between different layers [6–9]. Manufacturing techniques lead to different pore defects in the form of morphology (e.g., pore size, shape, and topology) and spatial distribution (e.g., the nearest distance between neighbors). The porosity defect has a major

*Corresponding author.

Email address: sdeng9@wisc.edu (Shiguang Deng)

influence on the resultant mechanical properties. The need to incorporate the role of porosity in the analysis of manufactured components is pivotal.

Synthetic models of primitive geometries are often utilized to represent pore morphologies within matrix materials for simplicity. Waters [10] used spherical voids to represent pore geometries in magnesium alloys to characterize the void behaviors during damage accumulation. Prithivirajan and Sangid [11] employed spherical voids to investigate the critical pore size during dynamic loading conditions (metal fatigue) on selective laser melting (SLM) nickel based alloys. Recent advances in multiscale methods coupled with synthetic pore models allows to correlate local material porosity defects with global structural performance. Ghosh et al. [12] integrated ellipsoid shaped pores into an adaptive multi-level model with varying resolution on each scale. While this model included three levels (macro, meso, and microscopic analysis), coupling between different levels was accomplished through asymptotic homogenization. Considering that pores in nickel-based cast alloys have complex morphologies with convex and concave radii, Taxer et al. [13] developed a more sophisticated synthetic model by intersecting three identical perpendicular ellipsoids at a common geometric center. This model could represent pore spatial ramifications by adjusting aspect ratios of ellipsoids. However, such multilevel models often require significant memory allocation costs due to the frequent data exchange between scales [14].

Actual porosity characteristics can be captured by computed tomography (CT), a non-destructive detection method for the analysis of material internal defects. Pore morphology and distribution are reconstructed in 3D models through image processing of scanning data [15,16]. With CT as an enabling technology, researchers have tried to incorporate reconstructed porosity characteristics with finite element (FE) models, followed by a direct solve. For example, actual shapes and sizes of casting pores were characterized by light microscopy and reproduced in a FE model to correlate with local stress concentrators in [17]. Pore geometries reconstructed from tomography scans were integrated with a micromechanical model to predict their influence on elastoplastic behaviors [18]. A quantitative description of non-uniformly distributed pores was incorporated into a 3D micromechanical analysis in [19]. It was found that the distributions of local stress depend on pores' size, orientation, and spatial arrangement. Hangai and Kitahara [20] distinguished gas and shrinkage induced pores by fractal analyses in terms of individual shapes and congregated spatial distributions. It seems straight forward to solve porosity problems using actual geometries; however, numerical issues can arise; presence of small sized and irregularly shaped pores significantly increases meshing complexity and computational expense in FE models. As an example, let's consider the W-profile plate produced by HPDC which contains more than 1300 pores represented by red dots in Figure 1(a). In this example, small elements are generated in the vicinity of pore surfaces to address geometric adaptivity and element size transition, which not only results in a substantial mesh size but also raises element quality issues. For example, distorted or inverted elements [21] can be observed close to pore boundaries as shown in Figure 1(c). Ill-shaped elements can further deteriorate the global stiffness matrix in FE systems, leading to slow convergence or even failure [22].

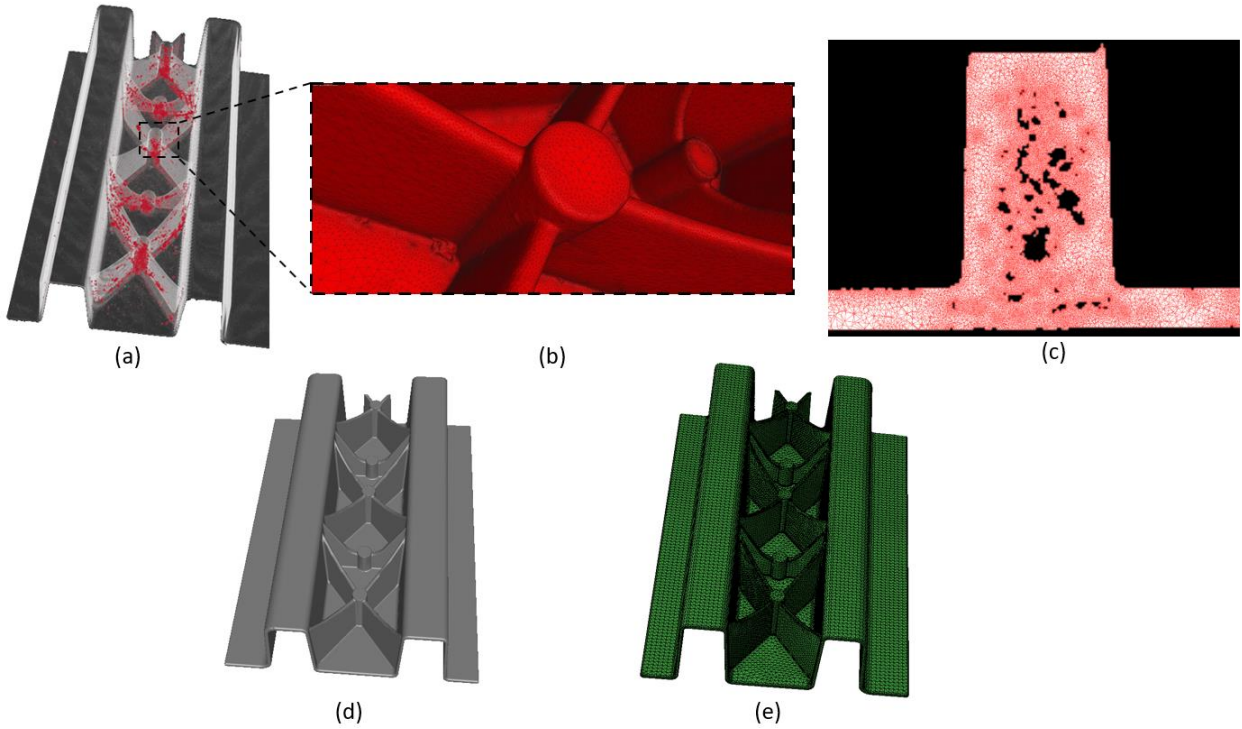


Figure 1: (a) Manufactured metallic component with more than 1300 pores whose morphologies and spatial distributions are reconstructed from 3D X-ray tomography; (b) an extremely fine FE mesh is created with more than 6.2 million tetrahedrons is created to capture the porous part's geometric details; (c) a cross-sectional view of the FE mesh illustrates the existence of irregularly shaped pores in close proximity and ill-shaped elements near pore surface; (d) a simplified (i.e., defeatured) model without any pores; and (e) a sufficiently fine mesh on the defeatured model only requires less than 0.25 million elements, i.e., about 4% of its porous counterpart.

Recent development in defeaturing techniques provide ways to efficiently integrate dimensional characteristics of pores. Defeaturing is a model simplification approach to preserve certain model properties during geometrical changes. Its basic idea is to work on a simplified model after removal of features and the performance difference (defeaturing error) between the fully featured and defeatured models is estimated via a posterior estimator. During defeaturing, various design sensitivities are utilized. Specifically, shape sensitivity can be used to compute the change in an arbitrary quantity of interest when models' boundary is subject to infinitesimal perturbations [23]; whereas topological sensitivity approximates the functional changes when an infinitesimally small hole is introduced onto a domain [24]. Li and Gao [25] estimated the error of suppressing arbitrarily sized geometric features by using adjoint theory where the feature can be negative (i.e., geometry cutout) or positive (i.e., geometry addition). In their later work [26], a second-order defeaturing method was proposed for error estimations when multiple interactive boundary features are suppressed. A limitation of this method is that it only accounts for boundary features but not for topological changes. Gopalakrishnan and Suresh [27] quantitatively analyzed the interval of defeaturing errors, whose bounds were approximated through monotonicity analysis. Turevsky et al. [28] developed a feature sensitivity by integrating shape sensitivities over geometric transformations to estimate the performance functions in a 2D Poisson problem where topological change was approximated by the shape sensitivity. In a recent work by Deng et al. [29], a first order defeaturing estimator was developed to exploit the morphology of manufacturing induced pores. To estimate the influence of pores on part behaviors, topological and shape

sensitivities were systematically integrated where each pore was assumed far away from neighbors so that interactions were neglected.

Despite much effort to incorporate the influence of porosity characteristics on structure performance, shortcomings and gaps remain.

- 1) Previous defeaturig methods mainly focus on removing one single isolated feature (e.g., void) from the design domain [27–29]. Since each feature is assumed as one term in a linear Taylor expansion, the effect of removing multiple features is addressed by simple additions without considering interactions among them. However, on actual manufactured components, pores are often clustered in close proximity, as shown in Figure 1(a) and (c). This dramatically increases pore-to-pore interactions and invalidates the presumed ‘*isolated*’ status. A more sophisticated approach is necessary to account for these interactions.
- 2) Synthetic pore models are not capable of representing actual pore morphologies, and multiscale methods are computationally expensive due to hierarchical material modeling on different scales. On the other hand, direct FE approaches which explicitly exploit tomography reconstructed porosity characteristics often experience difficulties in addressing meshing and convergent issues. There is a need for a computationally *efficient* framework to correlate tomography enabled 3D quantitative porosity data with structural performance.
- 3) Design sensitivities, e.g., size, shape or topological sensitivity, are mainly integrated into frameworks of structural optimization by providing gradient information [23,24,30]. To our best knowledge, this work is the first in its kind to utilize higher order design sensitivities to perform quantitative analysis on pore interactions.

Inspired by previous defeaturig methods, a novel second-order porosity-oriented estimator is proposed to predict metallic part behaviors due to porosity intrinsic characteristics. Its numerical advantage can be explained by the W-profile plate example in Figure 1(d) where the proposed method only requires solutions on a pore-free structure whose mesh size and quality are much improved as illustrated in Figure 1(e). Moreover, design sensitivities will be derived in boundary forms which only require the 2D surface mesh of pores, dramatically reducing computational costs compared to a classic FE analysis on 3D volume elements.

The remainder of the paper is organized as follows. Section 2 poses the problem statement and an overview of the proposed approach is given. Section 3 reviews topological sensitivity as background knowledge. Sections 4-7 details the development of the proposed method. In Section 8, the method is examined via numerous tests. Conclusion and future works are given in Section 9.

2. PROBLEM FORMULATION AND APPROACH OVERVIEW

In this section, we first formulate the porosity problem through mathematical statements and then provide a general overview of our proposed method, which, different from single feature suppression methods in [28,31], provides a second order defeaturig methodology to account for the impacts of pore-to-pore interactions on structural performances. Before proceeding to technical details, a summary of critical mathematical symbols and their meanings are given in Table 1. Based on this table, particular meaning of symbols should be understood from the context.

Table 1: Critical mathematical symbols and their meanings.

Symbol	Meaning
Ω	Geometry domain
Γ	Domain boundary
Ψ	Performance function
η, t, s	Shape parameters
ξ	Topological parameter
\mathbf{n}	Normal direction
\mathbf{x}	Points in current configuration
\mathbf{X}	Points in reference configuration
\mathbf{z}	Primary solution
λ	Adjoint solution
g	Generic function
σ	Stress
ϵ	Strain
C	Material tangent moduli
\mathbf{K}	Finite element stiffness matrix
\mathbf{f}	External load
L	Lagrangian equation
\mathbf{P}, \mathbf{Q}	Lagrangian multipliers
\mathbf{T}	Sensitivity field
D	Estimator value
\mathbf{T}	Shape transformation function
\mathbf{F}	Transformation tensor
V, W	Design speeds
\mathbf{J}	Jacobian of domain transformations
I_D	Effectivity index
U	Strain energy
E	External work
Π	Total potential energy

2.1 Problem formulation

Consider a smooth bounded domain [32] in 3D with two arbitrarily shaped pores in close distance in Figure 2. This porous domain can be viewed as the difference between a dense (or reference) domain Ω and the domains of two pores (Ω_{pi} and Ω_{pj}) as $\Omega - \Omega_{pi} - \Omega_{pj}$. If the boundary of the reference domain is Γ , then boundaries of the porous domain can be denoted as $\Gamma + \Gamma^{pi} + \Gamma^{pj}$. The inter-pore distance is considerably small such that the pore-to-pore interactions cannot be neglected.

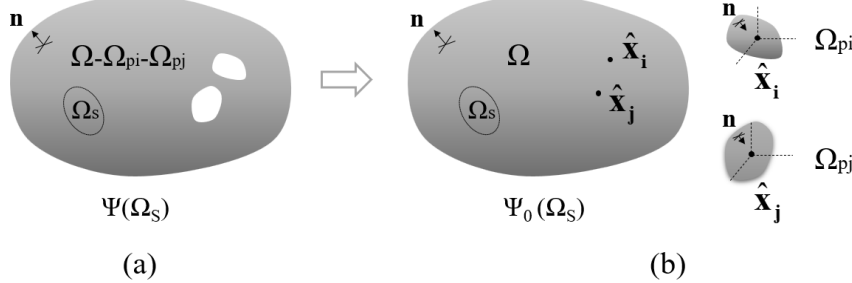


Figure 2: A porous domain with two closely distanced pores (a) can be viewed as the difference between a reference domain and domains of the two pores (b).

Two assumptions are made in this work to simplify our problems. First, the sizes of pores are much smaller than the domain. Second, the locations of pores are assumed far away from domain boundary to avoid surface effects, i.e.,

$$\|\Omega_p\| \ll \|\Omega\| \quad (2.1)$$

$$\|\Omega_p\| \ll \text{distance}(\Gamma, \Gamma^p) \quad (2.2)$$

With the above assumptions, we suppose a linear elastic boundary value problem [22] can be defined over the porous domain as

$$\begin{cases} -\nabla \cdot \boldsymbol{\sigma}(\mathbf{z}) = \mathbf{f}^b & \mathbf{x} \in \Omega - \Omega_{pi} - \Omega_{pj} \\ \mathbf{z} = \hat{\mathbf{z}} & \mathbf{x} \in \Gamma^h \\ \boldsymbol{\sigma}(\mathbf{z}) \cdot \mathbf{n} = \mathbf{f}^s & \mathbf{x} \in \Gamma^s \\ \boldsymbol{\sigma}(\mathbf{z}) \cdot \mathbf{n} = 0 & \mathbf{x} \in \Gamma^{pi}, \Gamma^{pj} \end{cases} \quad (2.3)$$

where the porous domain is subject to a body force \mathbf{f}^b , the displacement field \mathbf{z} is prescribed over the Dirichlet boundary Γ^h , a surface traction \mathbf{f}^s is applied on the Neumann boundary Γ^s with a unit outward normal vector \mathbf{n} , and a stress-free condition is assumed on the pore surfaces (Γ^{pi} and Γ^{pj}).

For linear elastic problems, we are often interested in a generic performance function defined in a desired region Ω_s as

$$\Psi = \iiint_{\Omega_s} g(\mathbf{z}) d\Omega \quad \Omega_s \subset \Omega - \Omega_{pi} - \Omega_{pj} \quad (2.4)$$

where g represents an arbitrary scalar function dependent on the displacement variable \mathbf{z} .

To solve $\Psi(\Omega_s)$ on a porous structure, directly solving Equation (2.3), e.g., through FE methods, seems straightforward. But several issues might arise. First, a real casting often contains many pores of complex morphologies. Generating FE volume mesh on such pore surfaces often leads to prohibitive meshing costs due to a large number of highly distorted elements. Ill-shaped elements further deteriorate global stiffness matrix in iterative solution process, leading to convergence problems. This direct FE approach should be therefore avoided.

On the other hand, if without any pore, it would be much easier to solve FE on the reference domain. Therefore, an alternative method is to develop a posterior estimator to predict the change of performance function in Equation (2.4) when pores are suppressed, i.e., a defeaturing process which considers pores as features in a FE model. Thus, a much simpler boundary value problem can be imposed on the reference domain as

$$\begin{cases} -\nabla \cdot \boldsymbol{\sigma}(\mathbf{z}) = \mathbf{f}^b & \mathbf{x} \in \Omega \\ \mathbf{z} = \hat{\mathbf{z}} & \mathbf{x} \in \Gamma^h \\ \boldsymbol{\sigma}(\mathbf{z}) \cdot \mathbf{n} = \mathbf{f}^s & \mathbf{x} \in \Gamma^s \end{cases} \quad (2.5)$$

where the quantity of interest is defined over the same region Ω_s as

$$\Psi_0 = \iiint_{\Omega_s} g(\mathbf{z}) d\Omega \quad \Omega_s \subset \Omega \quad (2.6)$$

From different boundary value problems in Equation (2.3) and (2.5), two different displacement solutions can be computed, which then results in two different values of performance functions in (2.4) and (2.6). If the quantity of interest is measured in an energy form, the difference (defeaturing error) between the two performance functions is called a global error, otherwise, a goal-oriented error [25]. Estimation of goal-oriented error is more important than its global counterpart, since it gives more insights into structural local effects, such as pointwise displacement or local stress concentration. However, goal-oriented error estimation is comparatively more difficult and expensive [25].

2.2 Approach overview

The objective of the proposed method is to estimate the quantity of interests $\Psi(\Omega_s)$ on a porous domain by using its counterpart $\Psi_0(\Omega_s)$ on a reference domain. To build connections between the two performance functions, a domain transformation can be proposed between the porous domain ($\Omega - \Omega_{pi} - \Omega_{pj}$) and the reference domain Ω as illustrated in Figure 3.

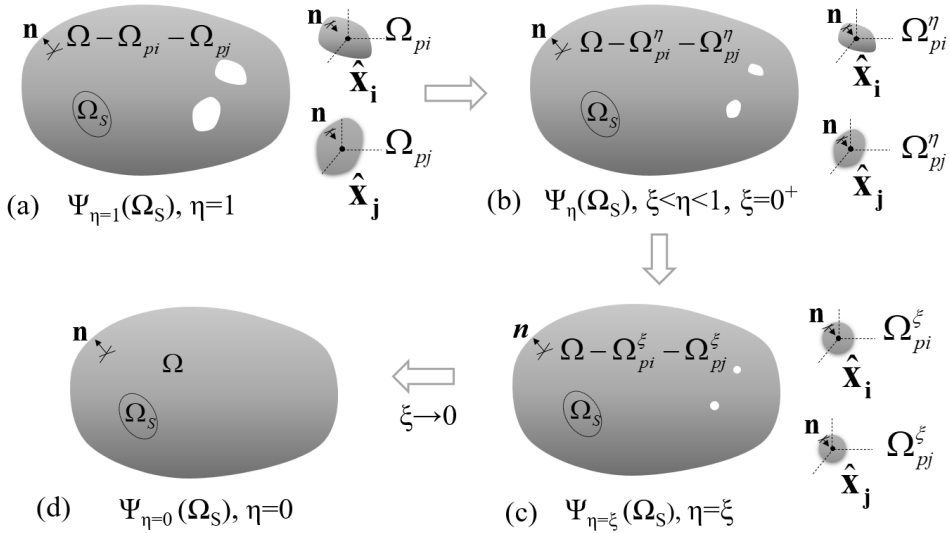


Figure 3: Schematic illustration of the proposed method.

In Figure 3, let the two pores both be parameterized by a continuous geometry parameter η on the interval $[0, 1]$. While the state ($\eta=1$) presents the full-sized pores as in Figure 3(a), the range ($0 < \eta < 1$) represents a continuously size-shrinking process for the two pores as in Figure 3(b). In this process, the first order shape sensitivity is employed to account for the variation of performance functions with respect to the shape change of each pore. The sensitivity field is supplemented by a second order shape sensitivity to quantify pore-to-pore interactions. At ($\eta=\xi$)

where $\xi \rightarrow 0^+$), we assume the two pores are scaled to infinitesimally small sizes (ξ) such that the influence of their original shapes can be assumed trivial as in Figure 3(c). If their shapes can be assumed as spheres of equivalent sizes ξ , removal of the two small spheres results in the reference domain as in Figure 3(d) where topological sensitivity is utilized to capture the impact of domain topological change. A detailed discussion about the relation between the topological and shape sensitivities can be found in [32].

In summary, the difference (defeaturing error) between the two performance functions in Equation (2.4) of Figure 3(a) and Equation (2.6) of Figure 3(d) can be approximated by exploiting shape and topological sensitivities as

$$\Psi(\Omega_s) - \Psi_0(\Omega_s) = \mathcal{D}_{topo} + \mathcal{D}_{shape} \quad (2.7)$$

where \mathcal{D}_{topo} and \mathcal{D}_{shape} are the posterior error estimations from topological and shape sensitivities, respectively. It is noted that \mathcal{D}_{shape} contains effects from the first order and second order shape sensitivities together. Summation of the two sensitivity fields, we can define a porosity-oriented second order estimator \mathcal{D}_{pore} as

$$\mathcal{D}_{pore} \equiv \mathcal{D}_{topo} + \mathcal{D}_{shape} \quad (2.8)$$

In the next section, technical backgrounds upon which the proposed methodology is developed are reviewed first.

3. BACKGROUND

The proposed porosity-oriented estimator is an extension to topological sensitivity whose concept is reviewed in this section.

Topological sensitivity captures the first order impact of inserting an infinitesimally small spherical hole within a domain on various quantities of interests [32–39].

Let a quantity of interest $\Psi_0(\Omega_s)$ be defined within a region of interests Ω_s on a smooth bounded domain Ω in Figure 4. Suppose an infinitesimally small hole with radius ξ is introduced by perturbing the domain Ω at an arbitrary location $\hat{\mathbf{x}}$. A new domain is then generated $(\Omega - \Omega_p^\xi)$ with boundary $(\Gamma + \Gamma_p^\xi)$. Given the topological change, the performance function defined in the same region Ω_s but on the perturbed domain can be written as [32]

$$\Psi_\xi(\Omega_s) = \Psi_0(\Omega_s) + g(\xi) \mathcal{T}_{topo}(\hat{\mathbf{x}}) + R(g(\xi)) \quad (3.1)$$

in which $g(\xi)$ is a monotone function whose value tends to zero as ξ approaches zero. $\mathcal{T}_{topo}(\bullet)$ is the first-order topological derivative defined at the hole location, and $R(\bullet)$ contains all higher order terms.

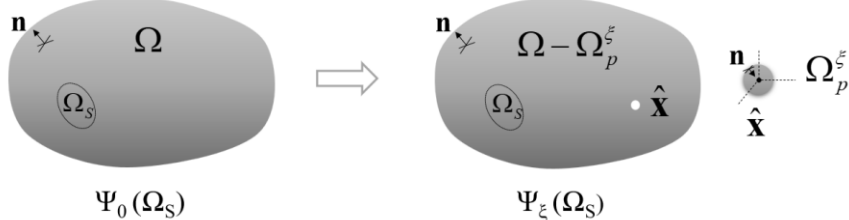


Figure 4: Illustration of a topological change in a smooth bounded 3D domain.

If we drop the higher order terms from Equation (3.1), it can be rewritten as the classic topological sensitivity as

$$\mathcal{T}_{topo}(\hat{\mathbf{x}}) \equiv \lim_{\xi \rightarrow 0} \frac{\Psi_\xi(\Omega_s) - \Psi_0(\Omega_s)}{g(\xi)} \quad (3.2)$$

where the monotone function $g(\xi)$ is taken as the volume of the small spherical hole [32].

To find the closed-form expression for the topological sensitivity, one must first define an adjoint. Recall that the adjoint field associated with a quantity of interest satisfies [23,40]:

$$\mathbf{K}\lambda = -\nabla_z \Psi \quad (3.3)$$

where \mathbf{K} is the stiffness matrix in a linear FE system and λ is the adjoint solution. The right-hand side of Equation (3.3), i.e., adjoint loads, can be symbolically determined by distribution theory [41].

Once the adjoint is computed, topological derivative can be computed on any point over the entire reference domain Ω [32]

$$\mathcal{T}_{topo}(\hat{\mathbf{x}}) = \frac{3}{4} \frac{1-\nu}{7-5\nu} \left[10\boldsymbol{\sigma}(\mathbf{z}) : \boldsymbol{\varepsilon}(\lambda) - \frac{1-5\nu}{1-2\nu} \text{tr}[\boldsymbol{\sigma}(\mathbf{z})] \text{tr}[\boldsymbol{\varepsilon}(\lambda)] \right] \quad (3.4)$$

To put things in perspective, once we obtain an analytical expression of topological sensitivity, e.g., through Equation (3.4), an arbitrary quantity of interests on the porous structure with an (infinitesimally) small spherical pore can be approximated by neglecting higher order terms from Equation (3.1) as:

$$\Psi(\Omega_s) \approx \Psi_0(\Omega_s) + \text{Vol}(\xi) \mathcal{T}_{topo}(\hat{\mathbf{x}}) \quad (3.5)$$

where $\text{Vol}(\xi)$ is the volume of the included small spherical pore.

Since there is no shape transformation effects, i.e., D_{shape} of Equation (2.7), in the topological change process where a small spherical pore is removed, the topology sensitivity-based estimation can be obtained by comparing Equation (3.1) with Equation (2.7) as:

$$D_{topo} = \text{Vol}(\xi) \mathcal{T}_{topo}(\hat{\mathbf{x}}) \quad (3.6)$$

After the impacts of topological change is captured by Equation (3.6), the influence brought by pore shape transformations and pore-to-pore interactions, D_{shape} of Equation (2.7), are developed in the next two sections.

4. DOMAIN TRANSFORMATION

The domain transformations described in Figure 3 necessitates the definition of design velocity on perturbed pore boundary, which is introduced in the following section.

4.1 Design velocity

Consider a smooth bounded domain $(\Omega - \Omega_p^\eta)$ with a parameterized pore (Ω_p^η) located at an arbitrary point \mathbf{X}_c in Figure 5(a). If the pore is perturbed by an infinitely small amount $d\eta$, the new domain can be denoted as $(\Omega - \Omega_p^{\eta-d\eta})$ with the perturbed pore $\Omega_p^{\eta-d\eta}$ in Figure 5(b). Note that only one pore is considered in this section.

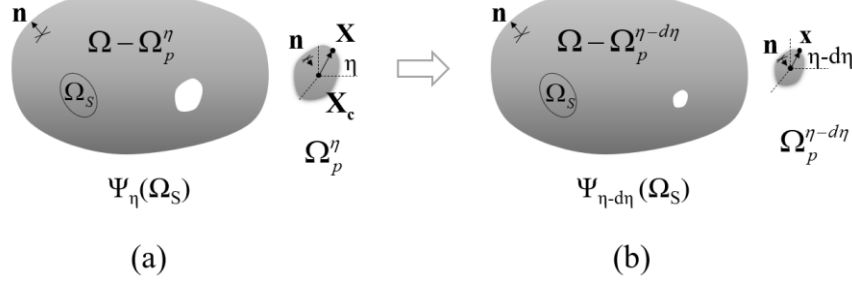


Figure 5: Domain transformation on the internal pore: parameterized geometry (a) and its perturbed counterpart (b).

If the mapping in Figure 5 is assumed smooth and invertible, it can be conveniently described by a domain transformation [23], where the original porous geometry is referred as a material domain on which an arbitrary point can be defined as \mathbf{X} , and the perturbed geometry can be described on the spatial domain whose points are denoted as \mathbf{x} .

If a shape parameter η can be used to denote the amount of geometry change in the direction of perturbation, then the shape transformation \mathbf{T} between the two domains in Figure 5 can be expressed by a linear and continuous mapping [23] as:

$$\mathbf{T}(\eta): [\Omega - \Omega_p^\eta](\mathbf{X}) \rightarrow [\Omega - \Omega_p^{\eta-d\eta}](\mathbf{x}) \quad (4.1)$$

For an arbitrary point on the pore surface, this mapping represents a scaling process where the size of pore is reduced by a small amount $d\eta$:

$$\mathbf{T}(\eta): \mathbf{x} = (\mathbf{X} - \mathbf{X}_c)\eta + \mathbf{X}_c \quad \mathbf{x} \in \Gamma_p \quad (4.2)$$

For any other points *not* on the pore surface, the mapping would not change its location:

$$\mathbf{T}(\eta): \mathbf{x} = \mathbf{X} \quad \mathbf{x} \notin \Gamma_p \quad (4.3)$$

By considering the amount of perturbation as pseudo time, a design velocity can therefore be defined as [23]

$$\mathbf{V} = \frac{d\mathbf{T}}{d\eta} \quad (4.4)$$

Specifically, the design velocity on pore surface can be computed as

$$\mathbf{V} = \mathbf{X} - \mathbf{X}_c \quad \mathbf{x} \in \Gamma_p \quad (4.5)$$

On the other hand, the velocity of points, which are not on pore surface, is assumed as zero

$$\mathbf{V} = \mathbf{0} \quad \mathbf{x} \notin \Gamma_p \quad (4.6)$$

4.2 Material derivative

Based on the aforementioned design velocity, a pointwise material derivative can be defined in the following manner with a perturbation of $\tau = d\eta$ [23]

$$\dot{\mathbf{z}} = \lim_{\tau \rightarrow 0} \left[\frac{\mathbf{z}_\tau(\mathbf{x} + \tau \mathbf{V}(\mathbf{x})) - \mathbf{z}(\mathbf{x})}{\tau} \right] = \mathbf{z}'(\mathbf{x}) + \nabla \mathbf{z} \mathbf{V}(\mathbf{x}) \quad (4.7)$$

where the spatial derivative is defined as

$$\mathbf{z}' = \lim_{\tau \rightarrow 0} \left[\frac{\mathbf{z}_\tau(\mathbf{x}) - \mathbf{z}(\mathbf{x})}{\tau} \right] \quad (4.8)$$

If a domain functional can be defined as an integral as,

$$\Psi = \iiint_{\Omega_\tau} g_\tau(\mathbf{x}_\tau) d\Omega_\tau \quad (4.9)$$

in which $g_\tau(x_\tau)$ is a scalar function defined on the perturbed domain Ω_τ , then its material derivative can be expressed as:

$$\Psi' \equiv \frac{d\Psi}{d\eta} = \iint_{\Omega} g'(\mathbf{x}) d\Omega + \iint_{\Gamma} g(\mathbf{x}) V_n d\Gamma \quad (4.10)$$

whereas V_n is the normal component of design speeds on the perturbed pore surfaces. Similarly, for a functional defined over a perturbed boundary surface Γ_τ ,

$$\Psi = \iint_{\Gamma_\tau} g_\tau(\mathbf{x}_\tau) d\Gamma_\tau \quad (4.11)$$

its material derivative can be expressed as

$$\Psi' \equiv \frac{d\Psi}{d\eta} = \iint_{\Gamma} \left[g'(\mathbf{x}) + (\nabla g^T \mathbf{n} + \Lambda g(x)) V_n \right] d\Gamma \quad (4.12)$$

wherein Λ is the mean of surface curvatures.

4.3 Weak formulation

A linear elastic problem defined over a porous geometry, e.g., in Figure 5(a), can be written in its strong form [22]

$$\begin{cases} -\nabla \cdot \boldsymbol{\sigma}(\mathbf{z}) = \mathbf{f}^b & \mathbf{x} \in \Omega \\ \mathbf{z} = \hat{\mathbf{z}} & \mathbf{x} \in \Gamma^h \\ \boldsymbol{\sigma}(\mathbf{z}) \cdot \mathbf{n} = \mathbf{f}^s & \mathbf{x} \in \Gamma^s \\ \boldsymbol{\sigma}(\mathbf{z}) \cdot \mathbf{n} = \mathbf{0} & \mathbf{x} \in \Gamma^P \end{cases} \quad (4.13)$$

where its solution space can be defined as

$$D_A = \left\{ \mathbf{z} \in C^2(\Omega) \mid \mathbf{z} = \hat{\mathbf{z}} \text{ on } \mathbf{x} \in \Gamma^h, \boldsymbol{\sigma} \cdot \mathbf{n} = \mathbf{f}^s \text{ on } \mathbf{x} \in \Gamma^s, \boldsymbol{\sigma} \cdot \mathbf{n} = \mathbf{0} \text{ on } \mathbf{x} \in \Gamma^P \right\} \quad (4.14)$$

For a linear elastic material with constitutive equation as

$$\boldsymbol{\sigma} = \mathbb{C} : \boldsymbol{\varepsilon} \quad (4.15)$$

where its strain is defined as

$$\boldsymbol{\varepsilon} = \frac{1}{2} (\nabla \mathbf{z} + \nabla \mathbf{z}^T) \quad (4.16)$$

Its strain energy and external work can be defined as

$$U(\mathbf{z}) = \frac{1}{2} \iiint_{\Omega} \boldsymbol{\sigma}(\mathbf{z}) : \boldsymbol{\varepsilon}(\mathbf{z}) d\Omega \quad (4.17)$$

$$E(\mathbf{z}) = \iiint_{\Omega} \mathbf{z}^T \mathbf{f}^b d\Omega + \iint_{\Gamma^s} \mathbf{z}^T \mathbf{f}^s d\Gamma \quad (4.18)$$

The total potential energy is defined as

$$\Pi(\mathbf{z}) = U(\mathbf{z}) - E(\mathbf{z}) \quad (4.19)$$

A displacement solution can be achieved by minimizing the total potential energy in an variational approach [18],

$$\delta\Pi(\mathbf{z}, \bar{\mathbf{z}}) = 0 = \delta U(\mathbf{z}, \bar{\mathbf{z}}) - \delta E(\mathbf{z}, \bar{\mathbf{z}}) \quad (4.20)$$

in which

$$a(\mathbf{z}, \bar{\mathbf{z}}) \equiv \delta U(\mathbf{z}, \bar{\mathbf{z}}) = \iiint_{\Omega} \boldsymbol{\sigma}(\mathbf{z}) : \boldsymbol{\varepsilon}(\bar{\mathbf{z}}) d\Omega \quad (4.21)$$

$$l(\bar{\mathbf{z}}) \equiv \delta E(\mathbf{z}, \bar{\mathbf{z}}) = \iiint_{\Omega} \bar{\mathbf{z}}^T \mathbf{f}^b d\Omega + \iint_{\Gamma^s} \bar{\mathbf{z}}^T \mathbf{f}^s d\Gamma \quad (4.22)$$

where the virtual arbitrary field $\bar{\mathbf{z}}$ is in a Hilbert space satisfying the kinematically admissible displacements as

$$Z = \left\{ \mathbf{z} \in H^1(\Omega) \mid \mathbf{z} = \mathbf{0} \text{ on } \Gamma^h \right\} \quad (4.23)$$

Then the solution of the strong formulation in Equation (4.13) can be computed by finding a solution $\mathbf{z} \in Z$ to

$$a(\mathbf{z}, \bar{\mathbf{z}}) = l(\bar{\mathbf{z}}) \quad (4.24)$$

If we assume both body force and surface tractions are independent of shape changes for the sake of simplicity

$$\mathbf{f}^b' = 0 \quad (4.25)$$

$$\mathbf{f}^s' = 0 \quad (4.26)$$

Taking material derivative of Equation (4.24) by invoking Equation (4.10) and (4.12) leads to

$$a'(\mathbf{z}, \bar{\mathbf{z}}) = l'(\bar{\mathbf{z}}) \quad (4.27)$$

in which

$$a'(\mathbf{z}, \bar{\mathbf{z}}) = \iiint_{\Omega} [\boldsymbol{\varepsilon}(\bar{\mathbf{z}}') : \boldsymbol{\sigma}(\mathbf{z}) + \boldsymbol{\varepsilon}(\bar{\mathbf{z}}) : \boldsymbol{\sigma}(\mathbf{z}')] d\Omega + \iint_{\Gamma} [\boldsymbol{\varepsilon}(\bar{\mathbf{z}}) : \boldsymbol{\sigma}(\mathbf{z})] V_n d\Gamma \quad (4.28)$$

and

$$l'(\bar{\mathbf{z}}) = \iiint_{\Omega} \mathbf{f}^{bT} \bar{\mathbf{z}}' d\Omega + \iint_{\Gamma^{f+s}} (\mathbf{f}^{bT} \bar{\mathbf{z}}) V_n d\Gamma + \iint_{\Gamma^s} \left\{ \mathbf{f}^{sT} \bar{\mathbf{z}}' + \left[\nabla (\mathbf{f}^{sT} \bar{\mathbf{z}})^T \mathbf{n} + \Lambda(\mathbf{f}^{sT} \bar{\mathbf{z}}) \right] \right\} V_n d\Gamma \quad (4.29)$$

where both $\dot{\mathbf{z}}$ and $\bar{\mathbf{z}}$ satisfy the kinematic admissible boundary condition in Equation (4.23).

A generic elastic quantity of interests can be defined over the porous domain in Figure 5(a) as

$$\Psi = \iiint_{\Omega_s} g(\mathbf{x}) d\Omega \quad (4.30)$$

where $g(\mathbf{x})$ is an arbitrary scalar function and the region of interest Ω_s is assumed fixed during transformation. We may have an interest in a pointwise displacement at the selected point $\hat{\mathbf{x}}$ as

$$\Psi_{nd} = \iiint_{\Omega} \delta(\mathbf{x} - \hat{\mathbf{x}}) \mathbf{z} d\Omega \quad (4.31)$$

It can be extended to other elastic quantity of interests, for example, elastic compliance or regional displacements [23]. By invoking Equation (4.10), its material derivative can be expressed as

$$\Psi_{nd}' = \iiint_{\Omega} \delta(\mathbf{x} - \hat{\mathbf{x}}) (\dot{\mathbf{z}} - \nabla \mathbf{z}^T \mathbf{V}) d\Omega \quad (4.32)$$

Its adjoint can be derived as

$$a(\lambda, \bar{\lambda}) = \iiint_{\Omega} \delta(\mathbf{x} - \hat{\mathbf{x}}) \bar{\lambda} d\Omega \quad (4.33)$$

Or, equivalently, in the form of partial differential equation through distribution theory [41]:

$$\begin{cases} -\nabla \cdot \boldsymbol{\sigma}(\lambda) = \delta(\mathbf{x} - \hat{\mathbf{x}}) & \mathbf{x} \in \Omega \\ \lambda = \mathbf{0} & \mathbf{x} \in \Gamma^h \\ \boldsymbol{\sigma}(\lambda) \cdot \mathbf{n} = \mathbf{0} & \mathbf{x} \in \Gamma^s, \Gamma^P \end{cases} \quad (4.34)$$

where the porous domain is only subject to a unit load at the point of interest as the adjoint body force. It should be noted the adjoint load definitions can be different for different performance function definitions in Equation (4.30).

Replacing the virtual displacement $\bar{\lambda}$ by $\dot{\mathbf{z}}$ in Equation (4.33) and equating with Equation(4.27), whose result is then inserted into Equation (4.32), results in the shape sensitivity of pointwise displacement in volume integral form. Interested readers can refer to Appendix or [23] for its exact expression.

It is noted that the sensitivity volume form is well suited for a general purpose design sensitivity analysis, especially in FE method [23]. However, shape sensitivity's boundary form is preferred in this work for several reasons. First, tomography reconstruction provides detailed geometric description on pore surfaces, which together with domain perturbations gives an excellent explanation of design velocity. Second, mesh generation and computation on a 2D surface mesh is much more efficient than a classic FE on a 3D volume mesh.

4.4 First order shape sensitivity

In this section, the shape sensitivity's domain form is further transformed to a boundary integral with the help of variational identities. The variational identity of the primary problem in Equation (4.13) can be obtained by multiplying a virtual displacement field $\bar{\mathbf{z}} \in Z$ and integrating by parts as

$$\iiint_{\Omega} \boldsymbol{\sigma}(\mathbf{z}) : \boldsymbol{\varepsilon}(\bar{\mathbf{z}}) d\Omega - \iiint_{\Omega} \mathbf{f}^b \cdot \bar{\mathbf{z}} d\Omega = \iint_{\Gamma} \bar{\mathbf{z}}^T (\boldsymbol{\sigma}(\mathbf{z}) \cdot \mathbf{n}) d\Gamma \quad (4.35)$$

In a similar approach, the variational identity of the adjoints in Equation (4.34) can be defined as

$$\iiint_{\Omega} \boldsymbol{\sigma}(\lambda) : \boldsymbol{\varepsilon}(\bar{\lambda}) d\Omega - \iiint_{\Omega} \bar{\lambda}^T \delta(\mathbf{x} - \hat{\mathbf{x}}) d\Omega = \iint_{\Gamma} \bar{\lambda}^T (\boldsymbol{\sigma}(\lambda) \cdot \mathbf{n}) d\Gamma \quad (4.36)$$

Substitute the two variational identities into the domain formulation and dropping all terms without associated design speeds, the shape sensitivity in boundary form can be obtained as

$$\Psi_{nd}' = \frac{d(\Psi_{\eta}(\Omega_s))}{d\eta} = - \iint_{\Gamma_{\eta}^P} [\boldsymbol{\sigma}(\mathbf{z}_{\eta}) : \boldsymbol{\varepsilon}(\lambda_{\eta})] V_n^{\eta} d\Gamma \quad (4.37)$$

where Γ_{η}^P refers to the parameterized (η) pore surfaces with normal design speeds V_n^{η} , $\boldsymbol{\sigma}(\mathbf{z}_{\eta})$ and $\boldsymbol{\varepsilon}(\lambda_{\eta})$ are the stress and strain fields on pore surface computed from primary and adjoint fields.

Since design speed is only defined over the boundary of pores, the boundary integration therefore only needs to be performed on pore surfaces. It is also noted that evaluation of Equation (4.37) requires solutions from both primary fields in Equation (4.13) and adjoints in Equation (4.34). Here, solving for adjoints would be trivial if the stiffness matrix associated with the primary problem is already factored, since the only difference between the two systems is the load definition which appears on the right-hand side of FE equations.

5. SECOND ORDER SHAPE SENSITIVITY

Second order shape sensitivities provide more descriptions on the influence of pore-to-pore interactions on desired performance functions. The target of this section is therefore to derive the second order shape sensitivities for the target function defined in Equation (4.31).

If we can use τ_t and τ_s to represent two infinitesimal perturbations on the boundaries of a pair of pores in close proximity as shown in Figure 6 where the two perturbations are associated with two design velocities \mathbf{V} and \mathbf{W} , respectively, then a two-parameter family of the perturbed domains (Ω_{ts}) can be defined by boundary transformations from a parameterized domain (Ω_η) as [42]:

$$\tilde{\mathbf{x}} = \mathbf{x} + t\mathbf{V}(\mathbf{x}) + s\mathbf{W}(\mathbf{x}), \quad \tilde{\mathbf{x}} \in \partial\Omega_{ts}, \quad \mathbf{x} \in \partial\Omega_\eta \quad (5.1)$$

with

$$\{\Omega_{ts}\}: (t, s) \in [(-\tau_t, +\tau_t), (-\tau_s, +\tau_s)] \quad (5.2)$$

where t and s are the two shape parameters defined on the two pores, respectively. It is clear that when $t=s=0$, the perturbed domain resembles the parameterized reference domain, i.e., $\Omega_{00}=\Omega_\eta$.

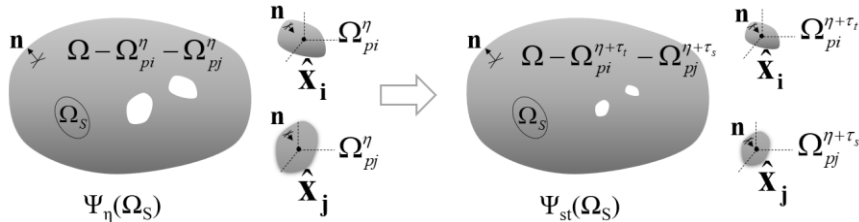


Figure 6: Domain transformations on two closely distanced pores.

If we define $\mathbf{U}(\Omega_{ts})$ as a suitable functional space on the perturbed domain, and $\mathbf{U}(\Omega_\eta)$ as a functional space on the parameterized domain Ω_η , similar to Section 4.3 the weak form on the perturbed domain as in Figure 6 can be written as

$$\tilde{a}(t, s; \tilde{\mathbf{z}}, \tilde{\mathbf{v}}) = \tilde{l}(t, s; \tilde{\mathbf{v}}), \quad \forall \tilde{\mathbf{v}} \in \mathbf{U}(\Omega_{ts}) \quad (5.3)$$

where

$$\tilde{a}(t, s; \tilde{\mathbf{z}}, \tilde{\mathbf{v}}) = \iiint_{\Omega_{ts}} \boldsymbol{\varepsilon}(\tilde{\mathbf{v}}) : \boldsymbol{\sigma}(\tilde{\mathbf{z}}) d\Omega_{ts} \quad (5.4)$$

$$\tilde{l}(t, s; \tilde{\mathbf{v}}) = \iiint_{\Omega_{ts}} \tilde{\mathbf{v}}^T \mathbf{f}^b d\Omega_{ts} + \iint_{\Gamma_{ts}} \tilde{\mathbf{v}}^T \mathbf{f}^s d\Gamma_{ts} \quad (5.5)$$

Also similar to Equation (4.30), on a perturbed domain Ω_{ts} , we are often interested in evaluating a performance function

$$\psi(t, s) \equiv \Psi(t, s; \tilde{\mathbf{z}}(t, s)) = \iiint_{\Omega_{ts}} g(\tilde{\mathbf{z}}(t, s)) d\Omega_{ts} \quad (5.6)$$

A transformation tensor \mathbf{F} can be therefore defined to connect the reference and perturbed domains and their associated functional spaces as

$$\mathbf{F} \equiv \frac{d\tilde{\mathbf{x}}}{dx} = \mathbf{I} + t\nabla\mathbf{V} + s\nabla\mathbf{W} \quad (5.7)$$

where the following properties of \mathbf{F} are used in the subsequent derivations

$$\begin{aligned} \left. \frac{\partial}{\partial t} (\mathbf{F}^{-1}) \right|_{t=s=0} &= -\nabla\mathbf{V}, & \left. \frac{\partial}{\partial s} (\mathbf{F}^{-1}) \right|_{t=s=0} &= -\nabla\mathbf{W} \\ \left. \frac{\partial}{\partial t} (|\mathbf{F}|) \right|_{t=s=0} &= \nabla \cdot \mathbf{V}, & \left. \frac{\partial}{\partial s} (|\mathbf{F}|) \right|_{t=s=0} &= \nabla \cdot \mathbf{W} \end{aligned} \quad (5.8)$$

By using the transformation tensor \mathbf{F} , the functions in Equation (5.3) can be transformed between a perturbed functional space and a parameterized space as

$$a(t, s; \mathbf{z}, \mathbf{v}) = l(t, s; \mathbf{v}), \quad \forall \mathbf{v} \in \mathbf{U}(\Omega_\eta) \quad (5.9)$$

where

$$a(t, s; \mathbf{z}, \mathbf{v}) = \frac{1}{4} \iiint_{\Omega_\eta} \left[(\mathbf{F}^{-T} \nabla \mathbf{v} + \nabla \mathbf{v}^T \mathbf{F}^{-1}) : \mathbb{C} : (\mathbf{F}^{-T} \nabla \mathbf{z} + \nabla \mathbf{z}^T \mathbf{F}^{-1}) |\mathbf{F}| \right] d\Omega_\eta \quad (5.10)$$

$$l(t, s; \mathbf{v}) = \iiint_{\Omega_\eta} \mathbf{v}^T \mathbf{f}^b |\mathbf{F}| d\Omega_\eta + \iint_{\Gamma_\eta} \mathbf{v}^T \mathbf{f}^s d\Gamma_\eta \quad (5.11)$$

Similar to Equation (4.31), a pointwise displacement is selected as the quantity of interest for demonstration purpose in Equation (5.12) as

$$\psi(t, s) = \Psi(t, s; \tilde{\mathbf{z}}) = \iiint_{\Omega_{ts}} \delta(\mathbf{x} - \hat{\mathbf{x}})^T \tilde{\mathbf{z}} d\Omega_{ts} = \iiint_{\Omega_\eta} \delta(\mathbf{x} - \hat{\mathbf{x}})^T \mathbf{z} |\mathbf{F}| d\Omega_\eta = \Psi(t, s; \mathbf{z}) \quad (5.12)$$

Gateaux derivatives [42] are also used to define functional derivatives in the second order sensitivity derivation, e.g., for an arbitrary function g ,

$$\langle D_3 g(t, s; \mathbf{z}); \mathbf{v} \rangle \equiv \lim_{\alpha \rightarrow 0} \frac{g(t, s; \mathbf{z} + \alpha \mathbf{v}) - g(t, s; \mathbf{z})}{\alpha} \quad (5.13)$$

$$\langle D_{33}^2 g(t, s; \mathbf{z}) : (\mathbf{v}, \mathbf{w}) \rangle \equiv \lim_{\beta \rightarrow 0} \frac{\langle D_3 g(t, s; \mathbf{z} + \beta \mathbf{w}); \mathbf{v} \rangle - \langle D_3 g(t, s; \mathbf{z}); \mathbf{v} \rangle}{\beta} \quad (5.14)$$

$$\langle D_{13}^2 g(t, s; \mathbf{z}); \mathbf{v} \rangle \equiv \lim_{\beta \rightarrow 0} \frac{\langle D_1 g(t, s; \mathbf{z} + \beta \mathbf{v}) \rangle - \langle D_1 g(t, s; \mathbf{z}) \rangle}{\beta} \quad (5.15)$$

$$\langle D_1 g(t, s; \mathbf{z}) \rangle \equiv \frac{\partial g}{\partial t} \quad (5.16)$$

where Equation (5.13) denotes the first order derivative of the functional with respect to its argument \mathbf{z} in the direction of a function \mathbf{v} . Its subindex '3' indicates \mathbf{z} is the third variable. Equation (5.14) is a second order Gateaux derivative with respect to its third argument \mathbf{z} in the directions of functions \mathbf{v} and \mathbf{w} , respectively. Similarly, Equation (5.15) defines a mixed second order partial derivative with respect to its first parameter t and a Gateaux derivative regarding its third argument \mathbf{z} in the direction of \mathbf{v} . Equation (5.16) represents a regular first order partial derivative with respect to one of its shape parameters.

5.1 Domain formulation

The derivation of shape sensitivity is often associated with the Lagrangian multiplier method [43]. For example, the first order shape sensitivity can be viewed as the derivative of the target function in Equation (5.12) with respect to a single shape parameter (t or s) but at the same time subject to the constraint that the field variable $\mathbf{z}(t,s)$ must satisfy the weak formulation in Equation (5.9). It is therefore natural to define a first order Lagrangian as

$$L(t, s; \mathbf{z}, \boldsymbol{\lambda}) = \Psi(t, s; \mathbf{z}) + a(t, s; \mathbf{z}, \boldsymbol{\lambda}) - l(t, s; \boldsymbol{\lambda}) \quad (5.17)$$

Taking the first derivatives of Equation (5.17) with respect to its two variables (\mathbf{z} and $\boldsymbol{\lambda}$), and vanishing the derivative results leads to

$$\frac{\partial \psi(t, s)}{\partial t} = \frac{\partial L(t, s; \mathbf{z}, \boldsymbol{\lambda})}{\partial t} \quad (5.18)$$

Solving the adjoint equation in Equation (5.18) would lead to the first order shape sensitivity in its domain form.

In a similar manner, for computing the second order shape sensitivity, a second order Lagrangian can be defined as

$$\begin{aligned} L_2(t, s; \mathbf{z}, \boldsymbol{\lambda}, \mathbf{P}, \mathbf{Q}) \\ = \frac{\partial L(t, s; \mathbf{z}, \boldsymbol{\lambda})}{\partial t} + [a(t, s; \mathbf{z}, \mathbf{P}) - l(t, s; \mathbf{P})] + [\langle D_3 a(t, s; \mathbf{z}, \boldsymbol{\lambda}); \mathbf{Q} \rangle + \langle D_3 \Psi(t, s; \mathbf{z}); \mathbf{Q} \rangle] \end{aligned} \quad (5.19)$$

where the second term on right hand side presents the constraint of variational equation in Equation (5.9) and the third term denotes the constraint of the adjoint in Equation (4.33). The two constraints are associated with two Lagrangian multipliers \mathbf{P} and \mathbf{Q} , respectively.

Therefore, computing the second order shape sensitivity boils down to taking derivative of the second order Lagrangian in Equation (5.19) within an open smooth interval $s \in (-\tau_s, +\tau_s)$ as [42]:

$$\frac{\partial^2 \psi(t, s)}{\partial t \partial s} = \frac{\partial L_2(t, s; \mathbf{z}, \boldsymbol{\lambda}, \mathbf{P}, \mathbf{Q})}{\partial s} \quad (5.20)$$

We then follow the procedures outlined in [42] to derive the two multipliers (\mathbf{P} and \mathbf{Q}) in subsequent derivations.

First, evaluation of multiplier \mathbf{Q} needs to solve

$$\langle D_3 a(t, s; \mathbf{z}, \boldsymbol{\lambda}); \mathbf{Q} \rangle = \frac{\partial l}{\partial t}(t, s; \boldsymbol{\lambda}) - \frac{\partial a}{\partial t}(t, s; \mathbf{z}, \boldsymbol{\lambda}), \quad \forall \boldsymbol{\lambda} \in U(\Omega_\eta) \quad (5.21)$$

where its terms can be transformed onto the parameterized domain (Ω_η) by setting $t=s=0$ as

$$\begin{aligned} \langle D_3 a(t, s; \mathbf{z}, \boldsymbol{\lambda}); \mathbf{Q} \rangle \Big|_{t=s=0} &= \frac{1}{4} \iiint_{\Omega_\eta} [(\nabla \boldsymbol{\lambda} + \nabla \boldsymbol{\lambda}^T) : \mathbb{C} : (\nabla \mathbf{Q} + \nabla \mathbf{Q}^T)] d\Omega_\eta \\ &= \iiint_{\Omega_\eta} \boldsymbol{\epsilon}(\boldsymbol{\lambda}) : \boldsymbol{\sigma}(\mathbf{Q}) d\Omega_\eta \end{aligned} \quad (5.22)$$

$$\frac{\partial l}{\partial t}(t, s; \boldsymbol{\lambda}) \Big|_{t=s=0} = \iiint_{\Omega_\eta} (\boldsymbol{\lambda}^T \mathbf{f}^b) \nabla \cdot \mathbf{V} d\Omega_\eta \quad (5.23)$$

$$\frac{\partial a}{\partial t}(t, s; \mathbf{z}, \boldsymbol{\lambda}) \Big|_{t=s=0} = \iiint_{\Omega_\eta} \left[\begin{aligned} & \boldsymbol{\varepsilon}(\boldsymbol{\lambda}) : \boldsymbol{\sigma}(\mathbf{z}) (\nabla \cdot \mathbf{V}) - \frac{1}{2} (\nabla \mathbf{V}^T \nabla \boldsymbol{\lambda} + \nabla \boldsymbol{\lambda}^T \nabla \mathbf{V}) : \boldsymbol{\sigma}(\mathbf{z}) \\ & - \frac{1}{2} \boldsymbol{\sigma}(\boldsymbol{\lambda}) : (\nabla \mathbf{V}^T \nabla \mathbf{z} + \nabla \mathbf{z}^T \nabla \mathbf{V}) \end{aligned} \right] d\Omega_\eta \quad (5.24)$$

Plugging Equations(5.22), (5.23) and (5.24) into Equation (5.21) leads to

$$\iiint_{\Omega_\eta} \boldsymbol{\varepsilon}(\boldsymbol{\lambda}) : \boldsymbol{\sigma}(\mathbf{Q}) d\Omega_\eta = \iint_{\Gamma_\eta} (\boldsymbol{\sigma}(\boldsymbol{\lambda}) \nabla \mathbf{z}^T \mathbf{V}) \cdot \mathbf{n} d\Gamma_\eta \quad (5.25)$$

where Equation (5.25) can be further simplified by the theory of distribution [41] as

$$\iiint_{\Omega_\eta} \boldsymbol{\varepsilon}(\boldsymbol{\lambda}) : \boldsymbol{\sigma}(\mathbf{Q}) d\Omega_\eta = - \iint_{\Gamma_\eta} \boldsymbol{\lambda} \cdot \left[\nabla \cdot \mathbb{C} : \left(\frac{1}{2} (\mathbf{A} + \mathbf{A}^T) \right) \right] d\Gamma_\eta \quad (5.26)$$

where,

$$\mathbf{A} = \mathbf{n} \otimes (\nabla \mathbf{z}^T \mathbf{V}) \quad (5.27)$$

Or, equivalently, Equation (5.26) can be written in its strong form as

$$\begin{cases} -\nabla \cdot \boldsymbol{\sigma}(\mathbf{Q}) = \mathbf{0} & \mathbf{x} \in \Omega - \Omega_p^\eta \\ \mathbf{Q} = \mathbf{0} & \mathbf{x} \in \Gamma^h \\ \boldsymbol{\sigma}(\mathbf{Q}) \mathbf{n} = \mathbf{0} & \mathbf{x} \in \Gamma^s \\ \boldsymbol{\sigma}(\mathbf{Q}) \mathbf{n} = -\nabla \cdot \mathbb{C} : \left(\frac{1}{2} (\mathbf{A} + \mathbf{A}^T) \right) & \mathbf{x} \in \Gamma_p^\eta \end{cases} \quad (5.28)$$

Evaluation of \mathbf{P} can be solved through

$$\begin{aligned} \langle D_3 a(t, s; \mathbf{z}, \mathbf{P}); \mathbf{v} \rangle &= - \left\langle D_{13}^2 \Psi(t, s; \mathbf{z}); \mathbf{v} \right\rangle \Big|_{t=s=0} - \left\langle D_{13}^2 a(t, s; \mathbf{z}, \boldsymbol{\lambda}); \mathbf{v} \right\rangle \Big|_{t=s=0} \\ &\quad - \left\langle D_{33}^2 a(t, s; \mathbf{z}, \boldsymbol{\lambda}); (\mathbf{Q}, \mathbf{v}) \right\rangle \Big|_{t=s=0} \\ &\quad - \left\langle D_{33}^2 \Psi(t, s; \mathbf{z}); (\mathbf{Q}, \mathbf{v}) \right\rangle \Big|_{t=s=0}, \quad \forall \mathbf{v} \in \mathbf{U}(\Omega_\eta) \end{aligned} \quad (5.29)$$

The terms in Equation (5.29) can be expanded as

$$\langle D_3 a(t, s; \mathbf{z}, \mathbf{P}); \mathbf{v} \rangle = \iiint_{\Omega_\eta} \boldsymbol{\varepsilon}(\mathbf{P}) : \boldsymbol{\sigma}(\mathbf{v}) d\Omega_\eta \quad (5.30)$$

$$\left\langle D_{13}^2 \Psi(t, s; \mathbf{z}); \mathbf{v} \right\rangle \Big|_{t=s=0} = \iiint_{\Omega_\eta} \delta(\mathbf{x} - \hat{\mathbf{x}})^T \mathbf{v} (\nabla \cdot \mathbf{V}) d\Omega_\eta \quad (5.31)$$

$$\left\langle D_{13}^2 a(t, s; \mathbf{z}, \boldsymbol{\lambda}); \mathbf{v} \right\rangle \Big|_{t=s=0} = \iiint_{\Omega_\eta} \left\{ \begin{aligned} & (\boldsymbol{\varepsilon}(\boldsymbol{\lambda}) : \boldsymbol{\sigma}(\mathbf{v})) \nabla \cdot \mathbf{V} \\ & - \frac{1}{2} (\nabla \mathbf{V}^T \nabla \boldsymbol{\lambda} + \nabla \boldsymbol{\lambda}^T \nabla \mathbf{V}) : \boldsymbol{\sigma}(\mathbf{v}) \\ & - \frac{1}{2} \boldsymbol{\sigma}(\boldsymbol{\lambda}) : (\nabla \mathbf{V}^T \nabla \mathbf{v} + \nabla \mathbf{v}^T \nabla \mathbf{V}) \end{aligned} \right\} d\Omega_\eta \quad (5.32)$$

Since both $a(t,s;\mathbf{z},\boldsymbol{\lambda})$ and $\Psi(t,s;\mathbf{z})$ are only linear in the field variable \mathbf{z} , their second Gateaux derivatives vanish

$$\left\langle D_{33}^2 a(t,s;\mathbf{z},\boldsymbol{\lambda}) : (\mathbf{Q}, \mathbf{v}) \right\rangle \Big|_{t=s=0} = 0 \quad (5.33)$$

$$\left\langle D_{33}^2 \Psi(t,s;\mathbf{z}) : (\mathbf{Q}, \mathbf{v}) \right\rangle \Big|_{t=s=0} = 0 \quad (5.34)$$

Plug Equations (5.30)-(5.34) to Equation (5.29), the value of multiplier \mathbf{P} can then be evaluated by

$$\iiint_{\Omega_\eta} \boldsymbol{\epsilon}(\mathbf{P}) : \boldsymbol{\sigma}(\mathbf{v}) d\Omega_\eta = - \iint_{\Gamma_\eta} \mathbf{v} \cdot \left[\nabla \cdot \mathbb{C} \left(\frac{1}{2} (\mathbf{B} + \mathbf{B}^T) \right) \right] d\Gamma_\eta \quad (5.35)$$

where,

$$\mathbf{B} = \mathbf{n} \otimes (\nabla \boldsymbol{\lambda}^T \mathbf{V}) \quad (5.36)$$

Equation (5.35) can be written in its strong form

$$\begin{cases} -\nabla \cdot \boldsymbol{\sigma}(\mathbf{P}) = \mathbf{0} & \mathbf{x} \in \Omega - \Omega_p^\eta \\ \mathbf{P} = \mathbf{0} & \mathbf{x} \in \Gamma^h \\ \boldsymbol{\sigma}(\mathbf{P}) \cdot \mathbf{n} = \mathbf{0} & \mathbf{x} \in \Gamma^s \\ \boldsymbol{\sigma}(\mathbf{P}) \cdot \mathbf{n} = -\nabla \cdot \mathbb{C} \left(\frac{1}{2} (\mathbf{B} + \mathbf{B}^T) \right) & \mathbf{x} \in \Gamma_p^\eta \end{cases} \quad (5.37)$$

To obtain the second order shape sensitivity, we compute the domain integral of $\langle D \langle D \Psi; \mathbf{V} \rangle; \mathbf{W} \rangle$,

$$\langle D \langle D \Psi; \mathbf{V} \rangle; \mathbf{W} \rangle = \langle D^2 \Psi : (\mathbf{V}, \mathbf{W}) \rangle + \langle D \Psi; (\nabla \mathbf{V}) \mathbf{W} \rangle \quad (5.38)$$

where the first term on the right side can be expanded as

$$\begin{aligned} \langle D^2 \Psi : (\mathbf{V}, \mathbf{W}) \rangle &= \frac{\partial^2 \Psi}{\partial t \partial s} (t, s; \mathbf{z}) \Big|_{t=s=0} + \frac{\partial^2 a}{\partial t \partial s} (t, s; \mathbf{z}, \boldsymbol{\lambda}) \Big|_{t=s=0} \\ &\quad - \frac{\partial^2 l}{\partial t \partial s} (t, s; \boldsymbol{\lambda}) \Big|_{t=s=0} + \frac{\partial a}{\partial s} (t, s; \mathbf{z}, \mathbf{P}) \Big|_{t=s=0} - \frac{\partial l}{\partial s} (t, s; \mathbf{P}) \Big|_{t=s=0} \\ &\quad + \langle D_{23}^2 a (t, s; \mathbf{z}, \boldsymbol{\lambda}); \mathbf{Q} \rangle \Big|_{t=s=0} + \langle D_{23}^2 \Psi (t, s; \mathbf{z}); \mathbf{Q} \rangle \Big|_{t=s=0} \end{aligned} \quad (5.39)$$

where each term can be further expanded in the domain integral forms as:

$$\frac{\partial \Psi}{\partial t} (t, s; \mathbf{z}) \Big|_{t=s=0} = \iiint_{\Omega_\eta} [\delta(\mathbf{x} - \hat{\mathbf{x}}) \mathbf{z}] \nabla \cdot \mathbf{V} d\Omega_\eta \quad (5.40)$$

$$\frac{\partial^2 \Psi}{\partial t \partial s} (t, s; \mathbf{z}) \Big|_{t=s=0} = \mathbf{0} \quad (5.41)$$

$$\frac{\partial l}{\partial t} (t, s; \boldsymbol{\lambda}) \Big|_{t=s=0} = \iiint_{\Omega_\eta} (\boldsymbol{\lambda}^T \mathbf{f}^b) \nabla \cdot \mathbf{V} d\Omega_\eta \quad (5.42)$$

$$\left. \frac{\partial^2 l}{\partial t \partial s}(t, s; l) \right|_{t=s=0} = \mathbf{0} \quad (5.43)$$

$$\begin{aligned} \left. \frac{\partial^2 a}{\partial t \partial s}(t, s; \mathbf{z}, \boldsymbol{\lambda}) \right|_{t=s=0} &= \iiint_{\Omega_\eta} \nabla \cdot \mathbf{V} \begin{bmatrix} -\frac{1}{2} (\nabla \mathbf{W}^T \nabla \boldsymbol{\lambda} + \nabla \boldsymbol{\lambda}^T \nabla \mathbf{W}) : \boldsymbol{\sigma}(\mathbf{z}) \\ -\frac{1}{2} \boldsymbol{\sigma}(\boldsymbol{\lambda}) : (\nabla \mathbf{W}^T \nabla \mathbf{z} + \nabla \mathbf{z}^T \nabla \mathbf{W}) \end{bmatrix} d\Omega_\eta \\ &+ \iiint_{\Omega_\eta} \nabla \cdot \mathbf{W} \begin{bmatrix} -\frac{1}{2} (\nabla \mathbf{V}^T \nabla \boldsymbol{\lambda} + \nabla \boldsymbol{\lambda}^T \nabla \mathbf{V}) : \boldsymbol{\sigma}(\mathbf{z}) \\ -\frac{1}{2} \boldsymbol{\sigma}(\boldsymbol{\lambda}) : (\nabla \mathbf{V}^T \nabla \mathbf{z} + \nabla \mathbf{z}^T \nabla \mathbf{V}) \end{bmatrix} d\Omega_\eta \end{aligned} \quad (5.44)$$

$$\begin{aligned} &+ \iiint_{\Omega_\eta} \nabla \cdot \mathbf{W} \begin{bmatrix} \frac{1}{4} (\nabla \mathbf{V}^T \nabla \boldsymbol{\lambda} + \nabla \boldsymbol{\lambda}^T \nabla \mathbf{V}) : \mathbb{C} : \\ (\nabla \mathbf{W}^T \nabla \mathbf{z} + \nabla \mathbf{z}^T \nabla \mathbf{W}) \end{bmatrix} d\Omega_\eta \\ &+ \iiint_{\Omega_\eta} \nabla \cdot \mathbf{W} \begin{bmatrix} \frac{1}{4} (\nabla \mathbf{W}^T \nabla \boldsymbol{\lambda} + \nabla \boldsymbol{\lambda}^T \nabla \mathbf{W}) : \mathbb{C} : \\ (\nabla \mathbf{V}^T \nabla \mathbf{z} + \nabla \mathbf{z}^T \nabla \mathbf{V}) \end{bmatrix} d\Omega_\eta \end{aligned}$$

$$\begin{aligned} \left. \frac{\partial a}{\partial s}(t, s; \mathbf{z}, \mathbf{P}) \right|_{t=s=0} &= \iiint_{\Omega_\eta} (\boldsymbol{\varepsilon}(\mathbf{P}) : \boldsymbol{\sigma}(\mathbf{z})) \nabla \cdot \mathbf{W} d\Omega_\eta \\ &- \frac{1}{2} \iiint_{\Omega_\eta} (\nabla \mathbf{W}^T \nabla \mathbf{P} + \nabla \mathbf{P}^T \nabla \mathbf{W}) : \boldsymbol{\sigma}(\mathbf{z}) d\Omega_\eta \\ &- \frac{1}{2} \iiint_{\Omega_\eta} \boldsymbol{\sigma}(\mathbf{P}) : (\nabla \mathbf{W}^T \nabla \mathbf{z} + \nabla \mathbf{z}^T \nabla \mathbf{W}) d\Omega_\eta \end{aligned} \quad (5.45)$$

$$\left. \frac{\partial l}{\partial s}(t, s; \mathbf{P}) \right|_{t=s=0} = \iiint_{\Omega_\eta} (\mathbf{P}^T \mathbf{f}^b) \nabla \cdot \mathbf{W} d\Omega_\eta \quad (5.46)$$

$$\begin{aligned} \left. \langle D_{23}^2 a(t, s; \mathbf{z}, \boldsymbol{\lambda}); \mathbf{Q} \rangle \right|_{t=s=0} &= \iiint_{\Omega_\eta} \begin{bmatrix} (\boldsymbol{\varepsilon}(\boldsymbol{\lambda}) : \boldsymbol{\sigma}(\mathbf{Q})) \nabla \cdot \mathbf{W} \\ -\frac{1}{2} (\nabla \mathbf{W}^T \nabla \boldsymbol{\lambda} + \nabla \boldsymbol{\lambda}^T \nabla \mathbf{W}) : \boldsymbol{\sigma}(\mathbf{Q}) \\ -\frac{1}{2} \boldsymbol{\sigma}(\boldsymbol{\lambda}) : (\nabla \mathbf{W}^T \nabla \mathbf{Q} + \nabla \mathbf{Q}^T \nabla \mathbf{W}) \end{bmatrix} d\Omega_\eta \end{aligned} \quad (5.47)$$

$$\left. \langle D_{23}^2 \Psi(t, s; \mathbf{z}); \mathbf{Q} \rangle \right|_{t=s=0} = \iiint_{\Omega_\eta} \left[\delta(\mathbf{x} - \hat{\mathbf{x}})^T \mathbf{Q} \right] \nabla \cdot \mathbf{W} d\Omega_\eta \quad (5.48)$$

The second term on the right side of Equation (5.38) can also be written in a volume integration form as

$$\begin{aligned}
& \langle D\psi; (\nabla \mathbf{V}) \mathbf{W} \rangle \\
&= \iiint_{\Omega_\eta} \left[\delta(\mathbf{x} - \hat{\mathbf{x}})^T \mathbf{z} \right] \nabla \cdot ((\nabla \mathbf{V}) \mathbf{W}) d\Omega_\eta + \iiint_{\Omega_\eta} \left\{ \begin{bmatrix} \boldsymbol{\varepsilon}(\boldsymbol{\lambda}) : \boldsymbol{\sigma}(\mathbf{z}) - \boldsymbol{\lambda}^T \mathbf{f}^b \\ -\nabla \boldsymbol{\lambda} : \boldsymbol{\sigma}(\mathbf{z}) - \nabla \mathbf{z} : \boldsymbol{\sigma}(\boldsymbol{\lambda}) \end{bmatrix} \right\} \nabla \cdot ((\nabla \mathbf{V}) \mathbf{W}) d\Omega_\eta \\
&= \iiint_{\Omega_\eta} \left[\delta(\mathbf{x} - \hat{\mathbf{x}})^T \mathbf{z} + \mathbf{N} \right] \Theta d\Omega_\eta + \iiint_{\Omega_\eta} \left[(\delta(\mathbf{x} - \hat{\mathbf{x}})^T \mathbf{z}) \nabla \mathbf{V} + \mathbf{N} \nabla \mathbf{V} \right] : \nabla \mathbf{W} d\Omega_\eta
\end{aligned} \tag{5.49}$$

where,

$$\mathbf{N} = \boldsymbol{\varepsilon}(\boldsymbol{\lambda}) : \boldsymbol{\sigma}(\mathbf{z}) - \boldsymbol{\lambda}^T \mathbf{f}^b - \nabla \boldsymbol{\lambda} : \boldsymbol{\sigma}(\mathbf{z}) - \nabla \mathbf{z} : \boldsymbol{\sigma}(\boldsymbol{\lambda}) \tag{5.50}$$

$$\Theta = \frac{\partial^2 V_j}{\partial x_i \partial x_i} W_j \tag{5.51}$$

Plugging Equations (5.39)-(5.51) to (5.38) leads to a volume integration of $\langle D\langle D\psi; \mathbf{V} \rangle; \mathbf{W} \rangle$:

$$\begin{aligned}
\langle D\langle D\psi; \mathbf{V} \rangle; \mathbf{W} \rangle &= \iiint_{\Omega_\eta} \left[(\delta(\mathbf{x} - \mathbf{X})^T \mathbf{z}) \nabla \mathbf{V} + \mathbf{M} \right] : \nabla \mathbf{W} d\Omega_\eta + \iiint_{\Omega_\eta} \left[\delta(\mathbf{x} - \mathbf{X})^T \mathbf{z} + \mathbf{N} \right] \Theta d\Omega_\eta
\end{aligned} \tag{5.52}$$

whereas interested reader are referred to Appendix or [42] for the exact expressions of \mathbf{M} .

5.2 Boundary formulation

In order to transform the second order shape sensitivity from its domain form to boundary form, we need to rely on the Guillaume-Masmoudi lemma [42], which states when a target function is only dependent on the shape of a domain, then the domain form in Equation (5.53) can be transformed to its boundary equivalence in Equation (5.54):

$$\langle D\psi(t, s); \mathbf{V} \rangle \Big|_{t=s=0} = \iiint_{\Omega_\eta} (\mathbf{G} : \nabla \mathbf{V} + \mathbf{h} \cdot \mathbf{V}) d\Omega_\eta \tag{5.53}$$

$$\langle D\psi(t, s); \mathbf{V} \rangle \Big|_{t=s=0} = \iint_{\Gamma_\eta} (\mathbf{G}^T \mathbf{V} \cdot \mathbf{n}) d\Gamma_\eta \tag{5.54}$$

where \mathbf{G} and \mathbf{h} are an arbitrary second order tensor and vector, respectively.

Then we can readily transform both Equations (5.49) and (5.52) from volume forms to their boundary forms. After dropping all terms without associated design velocities, the second order shape sensitivity with respect to the performance function defined in Equation (5.12) can be written in a boundary form on a parameterized domain (Ω_η) as

$$\begin{aligned}
\langle D^2\psi : (\mathbf{V}, \mathbf{W}) \rangle &= \langle D\langle D\psi; \mathbf{V} \rangle; \mathbf{W} \rangle - \langle D\psi; (\nabla \mathbf{V}) \mathbf{W} \rangle \\
&= \iint_{\Gamma_\eta^P} \begin{bmatrix} \boldsymbol{\varepsilon}(\mathbf{P}_\eta) : \boldsymbol{\sigma}(\mathbf{z}_\eta) \mathbf{I} + \boldsymbol{\varepsilon}(\mathbf{Q}_\eta) : \boldsymbol{\sigma}(\boldsymbol{\lambda}_\eta) \mathbf{I} \\ -\boldsymbol{\sigma}(\mathbf{P}_\eta) \nabla \mathbf{z}_\eta^T - \boldsymbol{\sigma}(\mathbf{z}_\eta) \nabla \mathbf{P}_\eta^T \\ -\boldsymbol{\sigma}(\mathbf{Q}_\eta) \nabla \boldsymbol{\lambda}_\eta^T - \boldsymbol{\sigma}(\boldsymbol{\lambda}_\eta) \nabla \mathbf{Q}_\eta^T \end{bmatrix} \mathbf{W} \cdot \mathbf{n} d\Gamma_\eta^P
\end{aligned} \tag{5.55}$$

6. SHAPE DEPENDENT PROBLEMS

After the topological and higher-order shape sensitivities are obtained, their accumulated effects through the transformation process in Figure 3 need to be accounted. The method starts with solving shape dependent problems.

6.1 Shape dependent problems

Let's use the geometry parameter η to generalize the boundary value problem on a porous domain. For a structure with fully sized pores ($\eta=1$):

$$\begin{cases} -\nabla \cdot \boldsymbol{\sigma}(\mathbf{z}) = \mathbf{f}^b & \mathbf{x} \in \Omega - \Omega_p \\ \mathbf{z} = \hat{\mathbf{z}} & \mathbf{x} \in \Gamma^h \\ \boldsymbol{\sigma}(\mathbf{z}) \cdot \mathbf{n} = \mathbf{f}^s & \mathbf{x} \in \Gamma^s \\ \boldsymbol{\sigma}(\mathbf{z}) \cdot \mathbf{n} = \mathbf{0} & \mathbf{x} \in \Gamma^p \end{cases} \quad (6.1)$$

For a porous structure with parameterized pores ($0 < \eta < 1$):

$$\begin{cases} -\nabla \cdot \boldsymbol{\sigma}(\mathbf{z}_\eta) = \mathbf{f}^b & \mathbf{x} \in \Omega - \Omega_p^\eta \\ \mathbf{z}_\eta = \hat{\mathbf{z}} & \mathbf{x} \in \Gamma^h \\ \boldsymbol{\sigma}(\mathbf{z}_\eta) \cdot \mathbf{n} = \mathbf{f}^s & \mathbf{x} \in \Gamma^s \\ \boldsymbol{\sigma}(\mathbf{z}_\eta) \cdot \mathbf{n} = \mathbf{0} & \mathbf{x} \in \Gamma_p^\eta \end{cases} \quad (6.2)$$

For a reference structure without pores ($\eta=0$):

$$\begin{cases} -\nabla \cdot \boldsymbol{\sigma}(\mathbf{z}) = \mathbf{f}^b & \mathbf{x} \in \Omega \\ \mathbf{z} = \hat{\mathbf{z}} & \mathbf{x} \in \Gamma^h \\ \boldsymbol{\sigma}(\mathbf{z}) \cdot \mathbf{n} = \mathbf{f}^s & \mathbf{x} \in \Gamma^s \end{cases} \quad (6.3)$$

It is noted when ($\eta=1$) the parameterized boundary value problem in Equation (6.2) resembles Equation(6.1), and when ($\eta=0$), the parameterized problem reduces to Equation (6.3).

Similarly, the quantity of interests defined in Equation (4.30) can also be parameterized, i.e., on a structure with full-size pore ($\eta=1$):

$$\Psi_1 = \iiint_{\Omega_s} g(\mathbf{z}) d\Omega \quad \Omega_s \subset \Omega - \Omega_p \quad (6.4)$$

For a porous structure with parameterized pores ($0 < \eta < 1$):

$$\Psi_\eta = \iiint_{\Omega_s} g(\mathbf{z}_\eta) d\Omega \quad \Omega_s \subset \Omega - \Omega_p^\eta \quad (6.5)$$

For a reference structure without pores ($\eta=0$):

$$\Psi_0 = \iiint_{\Omega_s} g(\mathbf{z}) d\Omega \quad \Omega_s \subset \Omega \quad (6.6)$$

In a similar manner, when ($\eta=1$), the parameterized performance function in Equation (6.5) resembles to that of a structure with full-size pore in Equation (6.4). At $\eta=0$, it is reduced to

Equation (6.6). The difference of the performance function between the fully sized porous state ($\eta=1$) and the reference state ($\eta=0$) can be expressed as

$$\Psi_1 - \Psi_0 = \mathcal{D}_{0 \leq \eta \leq 1} \Psi \quad (6.7)$$

where the range of the domain transformation can be divided into two stages: a pore size shrinking process ($\zeta \leq \eta \leq 1$) and an infinitesimally small hole removal process ($0 \leq \eta \leq \zeta$, $\zeta=0^+$), then the term on the right side of Equation (6.7) can be expanded accordingly as

$$\mathcal{D}_{0 \leq \eta \leq 1} \Psi = \mathcal{D}_{0 \leq \eta \leq \zeta} \Psi + \mathcal{D}_{\zeta \leq \eta \leq 1} \Psi \quad (6.8)$$

where the first term is a topological change process which, by invoking Equation (3.6), can be approximated by the topological sensitivity as

$$\mathcal{D}_{0 \leq \eta \leq \zeta} \Psi \equiv \mathcal{D}_{topo} = Vol(\zeta) \mathcal{T}(\hat{\mathbf{x}}) \quad (6.9)$$

The second term on the right side of Equation (6.8) is a shape changing process which can be further expanded as

$$\mathcal{D}_{\zeta \leq \eta \leq 1} \Psi \equiv \mathcal{D}_{shape} = \mathcal{D}_{shape}^1 + \mathcal{D}_{shape}^2 \quad (6.10)$$

In Equation (6.10), if the performance function is assumed continuously differentiable, then based on the fundamental theorem of calculus, it is readily to show the accumulated first order shape sensitivity during domain transformation process as

$$\mathcal{D}_{shape}^1 = \int_{\zeta}^1 \left(\frac{d\Psi_{\eta}}{d\eta} \right) d\eta \quad (6.11)$$

while the second term in Equation (6.10) is the second order shape sensitivity which can be computed as a summation of two terms as

$$\mathcal{D}_{shape}^2 = \mathcal{D}_{self}^2 + \mathcal{D}_{int}^2 \quad (6.12)$$

where,

$$\mathcal{D}_{self}^2 = \frac{1}{2} \int_{\zeta}^1 \left(\int_{\zeta}^1 \left(\frac{d^2\Psi_{\eta}}{d\eta_i d\eta_i} \right) d\eta_i \right) d\eta_j + \frac{1}{2} \int_{\zeta}^1 \left(\int_{\zeta}^1 \left(\frac{d^2\Psi_{\eta}}{d\eta_j d\eta_j} \right) d\eta_j \right) d\eta_i, \quad i \neq j \quad (6.13)$$

$$\mathcal{D}_{int}^2 = \int_{\zeta}^1 \left(\int_{\zeta}^1 \left(\frac{d^2\Psi_{\eta}}{d\eta_i d\eta_j} \right) d\eta_i \right) d\eta_j, \quad i \neq j \quad (6.14)$$

where i and j denote two different pores in a pair, and the \mathcal{D}_{shape}^1 and \mathcal{D}_{self}^2 terms only depend on single isolated pore (i or j) and represent its first and second order shape sensitivities. The term \mathcal{D}_{int}^2 depends on a pair of pores (i and j) and accounts for their interactive effects on performance functions.

It is noted to account for the integrands in Equation (6.10) needs primary solutions (\mathbf{z}) from Equation (4.13), adjoint solutions (λ) from Equation (4.34), and two Lagrangian multipliers (\mathbf{Q} and \mathbf{P}) from Equation (5.28) and (5.37), respectively. It is obvious all the variables are functions of the pore shape parameter η . Therefore, computing the shape integration in Equation (6.10) requires evaluations of integrant values for all η on $[\zeta, 1]$, which is impractical.

Therefore, in the following sections, we approximate the variables in Equation (6.10) as explicit functions of the shape parameter η . Then, through analytical integration, evaluation of Equation (6.10) become feasible.

6.2 Exterior approximations

The objective of this section is to use exterior formulation to approximate field variables on pore surfaces as an explicit function of shape parameter η .

The strong form of the elastostatic boundary value problem can be written on a reference domain as

$$\begin{cases} -\nabla \cdot \boldsymbol{\sigma}(\mathbf{z}_0) = \mathbf{f}^b & \mathbf{x} \in \Omega \\ \mathbf{z}_0 = \hat{\mathbf{z}} & \mathbf{x} \in \Gamma^h \\ \boldsymbol{\sigma}(\mathbf{z}_0) \cdot \mathbf{n} = \mathbf{f}^s & \mathbf{x} \in \Gamma^s \end{cases} \quad (6.15)$$

The same governing equations but on a porous structure with a parameterized pore can be written as

$$\begin{cases} -\nabla \cdot \boldsymbol{\sigma}(\mathbf{z}_\eta) = \mathbf{f}^b & \mathbf{x} \in \Omega - \Omega_p^\eta \\ \mathbf{z}_\eta = \hat{\mathbf{z}} & \mathbf{x} \in \Gamma^h \\ \boldsymbol{\sigma}(\mathbf{z}_\eta) \cdot \mathbf{n} = \mathbf{f}^s & \mathbf{x} \in \Gamma^s \\ \boldsymbol{\sigma}(\mathbf{z}_\eta) \cdot \mathbf{n} = \mathbf{0} & \mathbf{x} \in \Gamma_p^\eta \end{cases} \quad (6.16)$$

We assume there is a linear relation between the two displacement fields as

$$\mathbf{z}_\eta = \mathbf{z}_0 + \tilde{\mathbf{z}}_\eta \quad (6.17)$$

From constitutive equations of linear elastic materials,

$$\begin{cases} \boldsymbol{\sigma}_0 = \mathbb{C} : \boldsymbol{\varepsilon}_0 = \frac{1}{2} \mathbb{C} : (\nabla \mathbf{z}_0 + \nabla \mathbf{z}_0^T) \\ \boldsymbol{\sigma}_\eta = \mathbb{C} : \boldsymbol{\varepsilon}_\eta = \frac{1}{2} \mathbb{C} : (\nabla \mathbf{z}_\eta + \nabla \mathbf{z}_\eta^T) \end{cases} \quad (6.18)$$

It is ready to see that

$$\boldsymbol{\sigma}(\tilde{\mathbf{z}}_\eta) = \boldsymbol{\sigma}(\mathbf{z}_\eta - \mathbf{z}_0) = \boldsymbol{\sigma}(\mathbf{z}_\eta) - \boldsymbol{\sigma}(\mathbf{z}_0) \quad (6.19)$$

Combining Equation (6.15) with (6.16) and (6.19), it can be shown

$$\begin{cases} -\nabla \cdot \boldsymbol{\sigma}(\tilde{\mathbf{z}}_\eta) = \mathbf{0} & \mathbf{x} \in \Omega - \Omega_p^\eta \\ \tilde{\mathbf{z}}_\eta = \mathbf{0} & \mathbf{x} \in \Gamma^h \\ \boldsymbol{\sigma}(\tilde{\mathbf{z}}_\eta) \cdot \mathbf{n} = \mathbf{0} & \mathbf{x} \in \Gamma^s \\ \boldsymbol{\sigma}(\tilde{\mathbf{z}}_\eta) \cdot \mathbf{n} = -\boldsymbol{\sigma}_0 \cdot \mathbf{n} & \mathbf{x} \in \Gamma_p^\eta \end{cases} \quad (6.20)$$

Recall the assumptions in Equation (2.1) and (2.2). That is, if a pore is much smaller than the structure and it is located far away from structure surface, the residual field $\tilde{\mathbf{z}}_\eta$ in Equation (6.20) can be approximated by $\tilde{\mathbf{z}}_\eta^*$ in an exterior Neumann condition [44]:

$$\begin{cases} -\nabla \cdot \boldsymbol{\sigma}(\tilde{\mathbf{z}}_\eta^*) = \mathbf{0} & \mathbf{x} \in R^n - \Omega_p^\eta \\ \tilde{\mathbf{z}}_\eta^* = \mathbf{0} & \mathbf{x} \rightarrow \infty \\ \boldsymbol{\sigma}(\tilde{\mathbf{z}}_\eta^*) \cdot \mathbf{n} = -\boldsymbol{\sigma}_0 \cdot \mathbf{n} & \mathbf{x} \in \Gamma_p^\eta \end{cases} \quad (6.21)$$

The exterior approximation can be solved either through boundary element methods [45] or FEM with infinite elements [46].

Now consider the displacement field $\mathbf{z}(\mathbf{x}; \eta)$ defined over a parameterized spatial domain Ω_η . Its material representation but defined on the original (material) domain Ω_0 can be obtained by exploiting the transformation $\mathbf{x} = \mathbf{x}(\mathbf{X}; \eta)$. If we assume the displacement fields over the two domains are identical, i.e.,

$$\mathbf{z}(\mathbf{x}; \eta) = \mathbf{z}(\mathbf{X}; \eta) \quad (6.22)$$

where the points on spatial and material domain can be mapped through Equation (4.2). Then any point on the parameterized pore surface Γ_p^η can therefore be written as its material domain form

$$\Gamma_p^\eta = \eta \Gamma_p \quad (6.23)$$

where Γ_p refers to the fully scaled pore surface ($\eta=1$).

If we take gradients of the displacement field with respect to coordinates in two domains,

$$\nabla \mathbf{z}(\mathbf{x}) = \mathbf{J} \nabla \mathbf{Z}(\mathbf{X}) \quad (6.24)$$

where \mathbf{J} is the Jacobian matrix between the two domains. Combining Equation (6.18) with (6.24) it can be shown the relation of stress fields during the domain transformation is

$$\boldsymbol{\sigma}(\mathbf{x}) = \frac{1}{\eta} \boldsymbol{\sigma}(\mathbf{X}) \quad (6.25)$$

Substituting Equation (6.25) into (6.21) leads to:

$$\begin{cases} -\nabla \cdot \boldsymbol{\sigma}(\tilde{\mathbf{z}}_\eta^*(\mathbf{X})) = \mathbf{0} & \mathbf{X} \in R^n - \Omega_p^1 \\ \tilde{\mathbf{z}}_\eta^*(\mathbf{X}) = \mathbf{0} & \mathbf{X} \rightarrow \infty \\ \frac{1}{\eta} \boldsymbol{\sigma}(\tilde{\mathbf{z}}_\eta^*(\mathbf{X})) \cdot \mathbf{n} = -\boldsymbol{\sigma}_0 \cdot \mathbf{n} & \mathbf{X} \in \Gamma_p^1 \end{cases} \quad (6.26)$$

and let

$$\begin{cases} \mathbf{z}_E = \frac{1}{\eta} \tilde{\mathbf{z}}_\eta^*(\mathbf{X}) \\ \boldsymbol{\sigma}(\mathbf{z}_E) = \frac{1}{\eta} \boldsymbol{\sigma}(\tilde{\mathbf{z}}_\eta^*(\mathbf{X})) \end{cases} \quad (6.27)$$

plug into Equation (6.26), the exterior approximation can thus be formulated independently of the shape parameter η as:

$$\begin{cases} -\nabla \cdot \boldsymbol{\sigma}(\mathbf{z}_E) = \mathbf{0} & \mathbf{X} \in R^n - \Omega_p^1 \\ \mathbf{z}_E = \mathbf{0} & \mathbf{X} \rightarrow \infty \\ \boldsymbol{\sigma}(\mathbf{z}_E) \cdot \mathbf{n} = -\boldsymbol{\sigma}_0 \cdot \mathbf{n} & \mathbf{X} \in \Gamma_p^1 \end{cases} \quad (6.28)$$

The stress and strain fields can be written in an *explicit* form of the shape parameter η as:

$$\boldsymbol{\sigma}(\mathbf{z}_\eta(\mathbf{x})) \approx \boldsymbol{\sigma}(\mathbf{z}_0) + \boldsymbol{\sigma}(\tilde{\mathbf{z}}_\eta^*(\mathbf{x})) = \boldsymbol{\sigma}(\mathbf{z}_0) + \frac{1}{\eta} \eta \boldsymbol{\sigma}(\mathbf{z}_E(\mathbf{X})) = \boldsymbol{\sigma}(\mathbf{z}_0) + \boldsymbol{\sigma}(\mathbf{z}_E(\mathbf{X})) \quad (6.29)$$

$$\boldsymbol{\varepsilon}(\mathbf{z}_\eta(\mathbf{x})) \approx \boldsymbol{\varepsilon}(\mathbf{z}_0) + \boldsymbol{\varepsilon}(\mathbf{z}_E(\mathbf{X})) \quad (6.30)$$

The exterior equations can also be defined for *adjoints* as

$$\begin{cases} -\nabla \cdot \boldsymbol{\sigma}(\boldsymbol{\lambda}_E) = \mathbf{0} & \mathbf{X} \in R^n - \Omega_p^1 \\ \boldsymbol{\lambda}_E = \mathbf{0} & \mathbf{X} \rightarrow \infty \\ \boldsymbol{\sigma}(\boldsymbol{\lambda}_E) \cdot \mathbf{n} = -\boldsymbol{\sigma}_0 \cdot \mathbf{n} & \mathbf{X} \in \Gamma_p^1 \end{cases} \quad (6.31)$$

its stress and strain fields can thus be written as

$$\boldsymbol{\sigma}(\boldsymbol{\lambda}_\eta(\mathbf{x})) \approx \boldsymbol{\sigma}(\boldsymbol{\lambda}_0) + \boldsymbol{\sigma}(\boldsymbol{\lambda}_E(\mathbf{X})) \quad (6.32)$$

$$\boldsymbol{\varepsilon}(\boldsymbol{\lambda}_\eta(\mathbf{x})) \approx \boldsymbol{\varepsilon}(\boldsymbol{\lambda}_0) + \boldsymbol{\varepsilon}(\boldsymbol{\lambda}_E(\mathbf{X})) \quad (6.33)$$

In a similar manner, the parameterized multiplier \mathbf{Q}_η , on the pore surface of a porous structure $\Omega - \Omega_p^\eta$ can be solved by its strong form as

$$\begin{cases} -\nabla \cdot \boldsymbol{\sigma}(\mathbf{Q}_\eta(\mathbf{x})) = \mathbf{0} & \mathbf{x} \in \Omega - \Omega_p^\eta \\ \mathbf{Q}_\eta(\mathbf{x}) = \mathbf{0} & \mathbf{x} \in \Gamma^h \\ \boldsymbol{\sigma}(\mathbf{Q}_\eta(\mathbf{x})) \cdot \mathbf{n} = \mathbf{0} & \mathbf{x} \in \Gamma^s \\ \boldsymbol{\sigma}(\mathbf{Q}_\eta(\mathbf{x})) \cdot \mathbf{n} = -\nabla \cdot \mathbb{C} : \left(\frac{1}{2} (\mathbf{A} + \mathbf{A}^T) \right) & \mathbf{x} \in \Gamma_p^\eta \end{cases} \quad (6.34)$$

where

$$\mathbf{A} = \mathbf{n} \otimes (\nabla \mathbf{z}_\eta^T(\mathbf{x}) \mathbf{V}) \quad (6.35)$$

For the assumed linear mapping in Equation (4.2), it is readily to show

$$\boldsymbol{\sigma}(\mathbf{Q}_\eta(\mathbf{x})) = \frac{1}{\eta} \boldsymbol{\sigma}(\mathbf{Q}(\mathbf{X})) \quad (6.36)$$

$$\nabla \mathbf{Q}_\eta(\mathbf{x}) = \frac{1}{\eta} \nabla \mathbf{Q}(\mathbf{X}) \quad (6.37)$$

Plug Equations (6.36) and (6.37) into Equation(6.34) as

$$\begin{cases} -\nabla \cdot \sigma(Q(X)) = \mathbf{0} & X \in \Omega - \Omega_p^1 \\ Q(X) = \mathbf{0} & X \in \Gamma^h \\ \sigma(Q(X)) \cdot \mathbf{n} = \mathbf{0} & X \in \Gamma^s \\ \sigma(Q(X)) \cdot \mathbf{n} = -\nabla \cdot \mathbb{C} : \left(\frac{1}{2} (\bar{\mathbf{A}} + \bar{\mathbf{A}}^T) \right) & X \in \Gamma_p^1 \end{cases} \quad (6.38)$$

where

$$\bar{\mathbf{A}} = \mathbf{n} \otimes (\nabla \mathbf{z}^T(X) \mathbf{V}) \quad (6.39)$$

If we let

$$Q_E(X) = Q(X) \quad (6.40)$$

then similar to Equation (6.28), the solutions in Equation (6.38) can be approximated by an exterior Neumann formulation as

$$\begin{cases} -\nabla \cdot \sigma(Q_E(X)) = \mathbf{0} & X \in R^n - \Omega_p^1 \\ Q_E(X) = \mathbf{0} & X \rightarrow \infty \\ \sigma(Q_E(X)) \cdot \mathbf{n} = -\nabla \cdot \mathbb{C} : \left(\frac{1}{2} (\bar{\mathbf{A}} + \bar{\mathbf{A}}^T) \right) & X \in \Gamma_p^1 \end{cases} \quad (6.41)$$

Then the stress and displacement gradients of Q_η can be approximated by

$$\sigma(Q_\eta(x)) = \frac{1}{\eta} \sigma(Q_E(X)) \quad (6.42)$$

$$\nabla Q_\eta(x) = \frac{1}{\eta} \nabla Q_E(X) \quad (6.43)$$

Similarly, for the multiplier P_η in Equation (5.37), its stress and displacement gradients can be approximated as

$$\sigma(P_\eta(x)) = \frac{1}{\eta} \sigma(P_E(X)) \quad (6.44)$$

$$\nabla P_\eta(x) = \frac{1}{\eta} \nabla P_E(X) \quad (6.45)$$

7. SECOND ORDER POROSITY ESTIMATOR

Given the explicit forms of the topological sensitivity, the first order and second order shape sensitivities from previous sections, a gradient enhanced estimator is proposed in this section to predict the influence of the presence of closely distanced pores on an arbitrary elastic performance function.

7.1 Estimator formulation

Since all the variables in Equation (6.10) can be expressed as explicit functions of shape parameters η through exterior approximations, the integrations of the first order shape sensitivity in Equation (4.37) and the second order shape sensitivity in Equation (5.55) can therefore be computed, respectively, as:

$$\mathcal{D}_{shape}^1 = \int_{\Gamma_p} \left\{ -\frac{V_n}{2} [\boldsymbol{\sigma}_0(\mathbf{z}) + \boldsymbol{\sigma}_E(\mathbf{z})] : [\boldsymbol{\varepsilon}_0(\boldsymbol{\lambda}) + \boldsymbol{\varepsilon}_E(\boldsymbol{\lambda})] (1 - \xi^2) \right\} d\Gamma \quad (7.1)$$

and

$$\mathcal{D}_{shape}^2 = \iint_{\Gamma_p} \left[\begin{array}{l} [\boldsymbol{\sigma}_0(\mathbf{z}) + \boldsymbol{\sigma}_E(\mathbf{z})] : \boldsymbol{\varepsilon}_E(\mathbf{P}) \mathbf{I} + [\boldsymbol{\sigma}_0(\boldsymbol{\lambda}) + \boldsymbol{\sigma}_E(\boldsymbol{\lambda})] : \boldsymbol{\varepsilon}_E(\mathbf{Q}) \mathbf{I} \\ -\boldsymbol{\sigma}_E(\mathbf{P}) [\nabla \mathbf{z}_0 + \nabla \mathbf{z}_E]^T - [\boldsymbol{\sigma}_0(\mathbf{z}) + \boldsymbol{\sigma}_E(\mathbf{z})] \nabla \mathbf{P}_E^T \\ -\boldsymbol{\sigma}_E(\mathbf{Q}) [\nabla \boldsymbol{\lambda}_0 + \nabla \boldsymbol{\lambda}_E]^T - [\boldsymbol{\sigma}_0(\boldsymbol{\lambda}) + \boldsymbol{\sigma}_E(\boldsymbol{\lambda})] \nabla \mathbf{Q}_E^T \end{array} \right] \mathbf{W} \cdot \mathbf{n} (1 - \xi)^2 d\Gamma_p \quad (7.2)$$

The topological sensitivity-based estimator is reiterated as

$$\mathcal{D}_{topo} = Vol(\xi) \mathcal{T}_{topo}(\hat{\mathbf{x}}) \quad (7.3)$$

For a porous domain with two pores in close proximity, the topological and the first order shape sensitivity estimators in Equation (7.3) and (7.1) are computed for each pore, indicating their individual impacts on the studied quantity of interests. The second order shape sensitivity-based estimator in Equation (7.2) is computed for the pairwise pores, representing their interactive effects.

A typical manufactured metal component often contains many pores. The aforementioned estimators need to be extended to scenarios with multiple pores. Therefore, a gradient-enhanced porosity estimator can be computed by summing contributions from topological and higher order shape sensitivities as

$$\Psi(\Omega_S) \approx \Psi_0(\Omega_S) + \sum_{1 \leq i \leq n} (\mathcal{D}_{topo})_i + \sum_{1 \leq i \leq n} (\mathcal{D}_{shape}^1)_i + \sum_{1 \leq i \neq j \leq n} (\mathcal{D}_{shape}^2)_{i,j} \quad (7.4)$$

where n is the total number of pores, and i and j denote two different pores in a pair. In other words, a defeaturizing error can be defined as

$$D = \sum_{1 \leq i \leq n} (\mathcal{D}_{topo})_i + \sum_{1 \leq i \leq n} (\mathcal{D}_{shape}^1)_i + \sum_{1 \leq i \neq j \leq n} (\mathcal{D}_{shape}^2)_{i,j} \quad (7.5)$$

The proposed gradient enhanced estimator generally gives more precise predictions by including higher order sensitivity terms and inter-pore interactions at the cost of more computational expense. By ignoring higher order terms, Equation (7.4) reduces in the first order estimator [28,31] as

$$\Psi(\Omega_S) \approx \Psi_0(\Omega_S) + \sum_{1 \leq i \leq n} (\mathcal{D}_{topo})_i + \sum_{1 \leq i \leq n} (\mathcal{D}_{shape}^1)_i \quad (7.6)$$

where elastic performance function is estimated by simply adding up independently computed topological and shape sensitivities on each pore.

7.2 Proposed algorithm

Summarizing the preceding sections, the major steps for computing the proposed gradient enhanced estimator for multiple pores is described below.

- 1) *Prepare material preparation and collect data:* scan a manufactured component (Ω), and reconstruct its internal pores (Ω_p). The component's reference geometry ($\Omega-\Omega_p$) can be obtained either from tomography reconstruction or directly from CAD model.
- 2) *Compute topological sensitivity:* apply loading and boundary conditions on the reference structure ($\Omega-\Omega_p$) where primary solutions (\mathbf{z}) can be obtained by solving Equation (4.13) and adjoints (λ) from Equation(4.34). With the primary and adjoint solutions, topological sensitivity can be easily computed at each pore's center position on the reference structure, e.g., by Equation (3.4), and the topological sensitivity-based estimator (D_{topo}) can be computed by Equation (7.3).
- 3) *Compute the first order shape sensitivity:* approximate pore stress and strain by exterior formulation in Equation(6.29)-(6.33) based on the primary and adjoint solutions obtained from Step-2 at each pore. The design speed on pore boundaries can be computed by Equation (4.5). With the design speed and approximated primary and adjoint solutions, the first order shape sensitivity can be computed in Equation(4.37) and its integration in Equation (7.1).
- 4) *Compute the second order shape sensitivity:* compute two additional Lagrangian multipliers (\mathbf{Q} and \mathbf{P}) from Equation (5.28) and (5.37), and the second order shape sensitivity in Equation (6.12) and the integration of the second order shape sensitivity is then performed by Equation(7.2).
- 5) *Assemble the porosity estimator:* assemble the proposed gradient enhanced estimator from the sensitivities computed from above steps on every pore where inter-pore interactions are computed in each *pair* of pores. Finally, with the initial value of quantity of interests (Ψ_0) on the reference structure from Step-1, its value (Ψ) on the flawed structure with internal pores can be estimated by Equation (7.4).

8. NUMERICAL EXPERIMENTS

In this Section, the proposed method is demonstrated through several numerical experiments. The proposed porosity-oriented estimator has been implemented in Python for both 2D and 3D cases. The linear elastic problems in Equation (2.5) and (2.6) are solved in ABAQUS [47], a commercial FE package. The exterior approximation in Equation (6.28) is solved by FAST-BEM [45], a boundary element method package. Other software has also been utilized for image processing, geometry repair and mesh editing. Their applications are discussed in the sections where they are applied. All experiments were conducted on a 64-bit WINDOWS 10 machine with the following hardware: Intel I5-8250U CPU 4 cores running at 1.6 GHz with 16 GB of installed physical memory (RAM).

In all experiments, we neglect any metal polycrystalline microstructures (e.g., grain boundary, triple, or quad points) except for pores and we assume that materials are isotropic with perfect linear elastic properties (Young's modulus $E=6.89e10$ N/m², and Poisson's ratio $\nu=0.35$). The first example (Section 8.1) involves a 2D benchmark study where pore parameters are studied for their influence on the accuracy of the proposed method. The second example (Section 8.2) is a case study on a 2D bracket with a simulated pore spatial distribution. The third example (Section 8.3)

involves a 3D hook model where the pores are represented by synthetic models. The last example (Section 8.4) is on a real casting component with tomography reconstructed pore characteristics. Elastic quantities of interests are computed in each example, and the proposed second order estimator is then compared with two other estimators as well as solutions from direct FEA:

- 1) *Direct FEA*: a porous model is created first. The boundary value problems in Equation (2.3) is then solved. The value of performance function is denoted as Ψ . This approach is considered as the ground truth when comparing with estimators. However, it is computational expensive and hence should be avoided in practice.
- 2) *Topological sensitivity estimator*: field variables are solved on a reference domain where its quantity of interests is denoted as Ψ_0 . If each pore can be represented by an equivalent circle hole in 2D (or a sphere in 3D), the change of performance function can be approximated by multiplying topological sensitivity with the pore's equivalent area (or volume in 3D), denoted as D_{topo} in Equation (3.6). As shown in experiments, this approach is inaccurate and only used here for comparison.
- 3) *First order porosity sensitivity*: the estimation on the change of performance function (D^1_{pore}) can be computed in Equation (7.6) which takes pore characteristics (morphology and distribution) into account but neglect pore-to-pore interactions.
- 4) *Second order porosity estimator*: by combining the first order with the second order shape sensitivities, the change of quantity (i.e., defeaturing error) can be computed though Equation (7.4) and is denoted as D^2_{pore} . The accuracy of this estimator is proved better than the others in scenarios of closely clustered pores.

In order to quantify the accuracy of different estimators, an effectivity index can be defined as the ratio between the predicted change of quantity (i.e., defeaturing error) and the exact value [25] as

$$I_D = \frac{D}{\Psi - \Psi_0} \quad (8.1)$$

where D can be D_{topo} , D^1_{pore} , or D^2_{pore} . It is obvious that the closer to 1.0, the more accurate an estimator is. In the field of error estimation, for the quantities measured in global norm, if the effectivity indices are in the range between 0.5 and 2.0, it would be considered acceptable [25]. However, for a local quantity (e.g., pointwise displacement), the effectivity index for a good estimator can be relaxed up to 10.0, as it is generally more difficult and expensive to obtain [48].

8.1 Benchmark study

In this section, a 2D cantilever beam is used as a benchmark example to study the influences of various pore parameters on the proposed estimator.

8.1.1 Pore distance

In this example, we vary the distances between two pores to study the impact of distances on inter-pore interactions. As shown in Figure 7, the study is performed on a 2D cantilever beam with two identical circular pores. The dimension of the beam is 200 mm long and 100 mm wide. It is clamped on left edge and a vertical tip load with a magnitude of 1000 N is applied on its up-right corner. The quantity of interest in this study is the vertical displacement at the bottom right corner of the beam and its defeaturing error can be defined via Equation (7.5). While the radii of both pores are prescribed as 5 mm, their horizontal distance is varied from 1mm to 45 mm. It is

noteworthy pore sizes in benchmarks do not necessarily indicate the sizes of actual pores on manufacturing components. Their relative sizes compared with the beam are only utilized for the parameter study.

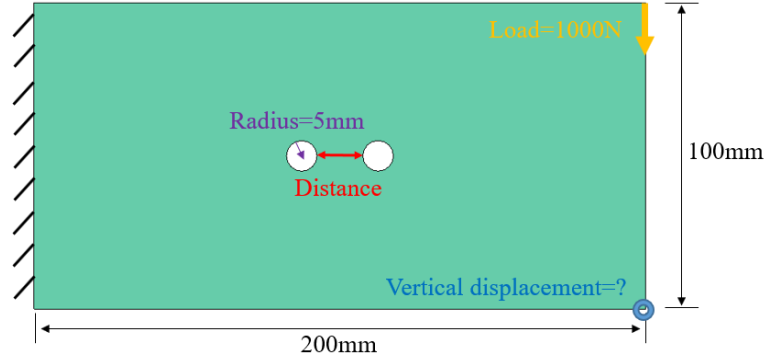


Figure 7: Dimensions and boundary conditions of the 2D cantilever beam with two closely distanced pores.

We compared the accuracies of three different estimators, i.e., D_{topo} , D_{pore}^I , and the proposed D_{pore}^2 , with respect to various pore-to-pore distances in Figure 8. It is evident when the distance is small (e.g., when distance is smaller than 5 mm), both D_{topo} and D_{pore}^I give much worse results than D_{pore}^2 , where the closer an effectivity index is to 1.0, the more accurate the estimator is. On the other hand, as the distance becomes larger (e.g., when distance is larger than 20 mm), all three estimators result in similarly good predictions in this example.

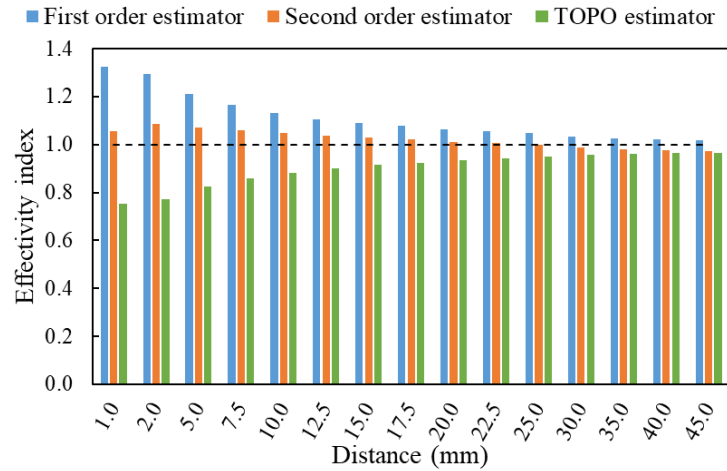


Figure 8: Effectivity indices of different estimators on the pore-to-pore distances study.

The observation, that the accuracies of D_{topo} and D_{pore}^I start to deteriorate as pores are in closer proximity, can be explained by the following reason. When the distance decreases, interactions between pores significantly increase, which is not able to be accounted by both aforementioned estimators. To verify this, the relation between pore-to-pore distances and values of interaction term in Equation (6.14) is plotted in Figure 9.

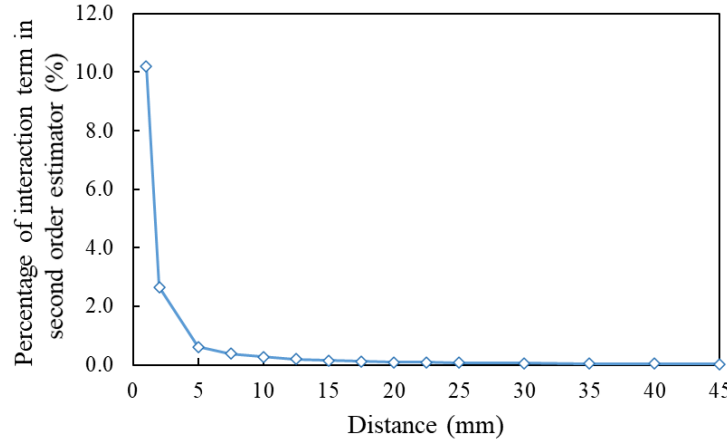


Figure 9: Relation between pore-to-pore distances and their interactions.

Figure 9 manifests a qualitative relationship between pore-to-pore interactions and distances. For example, when the distance between pore surfaces is as small as 1mm, the interaction can account for up to 10% of the proposed estimator. But as the distances increase, the interaction effect gradually drops to a neglectable level.

In order to have a better understanding of the contributions from each term in the proposed second order estimator, the percentage of each term in Equation (7.5) are compared in Figure 10 where the pore-to-pore distance is 1mm. It is observed the first order terms in Equation (7.1) account for 79.7%, and the second order terms together in Equation (7.2) account for about 20.3%. Specifically, the interaction term in Equation (6.14) accounts for 10.2%. It is noted the value from topological sensitivity-based term in Equation (7.3) is trivial (smaller than 0.01%) compared with others due a small ξ value we choose. Topological sensitivity is only used here to approximate a structural topology change where one (isolated and theoretically infinitesimally) small hole is introduced at each of the two pore locations. In a heuristic manner, we choose ξ as 1% of each pore's actual size. It should also be noted that with the change of inter-pore distances, the values of terms in Figure 10 are also subject to change.

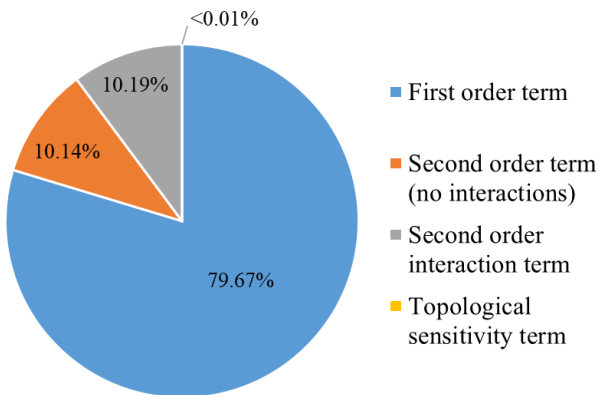


Figure 10: Percentages of different terms in the proposed second order estimator when the pore-to-pore distance is 1 mm in the model of Figure 7.

8.1.2 Pore size

The impact of pore sizes on the proposed estimator is studied in this benchmark example on a model in Figure 11. This example uses the same 2D cantilever beam as the previous study. In this example, the pore-to-pore distance is fixed as 1 mm but the radii of the two identical pores are varied from 1.5 mm to 10 mm. Again, the performance function is the vertical displacement at the right bottom corner.

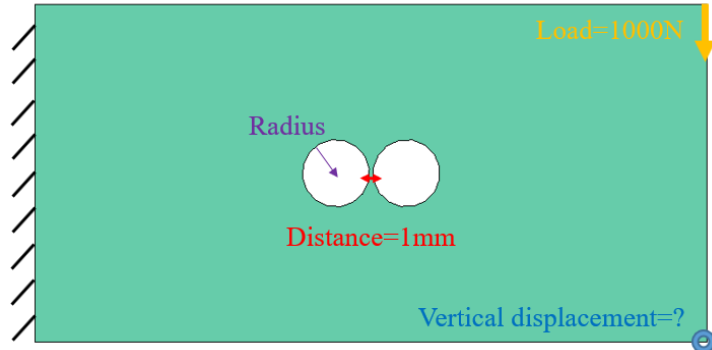


Figure 11: A 2D cantilever beam with boundary conditions and two pores with fixed distance.

The accuracies of the three estimators are compared regarding different pore sizes in Figure 12. In this study, since the pore-to-pore distance is kept the same, the larger pore sizes, the smaller ratio between inter-pore distances and pore sizes. Intuitively, a smaller ratio here represents a stronger pore-to-pore interaction. As in Figure 12, when the pore sizes increase, the accuracies of both D_{topo} and D^1_{pore} start to deteriorate while D^2_{pore} is still maintained at high fidelity. For example, when the pore radii are 10mm, the effectivity index of D^2_{pore} is 1.1 while the indices of D_{topo} and D^1_{pore} are 1.6 and 0.6, respectively. Their deteriorating accuracies can be explained by stronger pore-to-pore interactions which cannot be accounted by the two estimators.

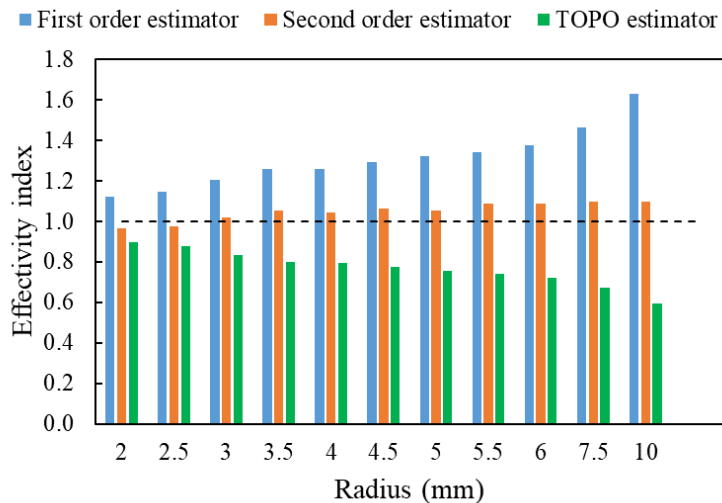


Figure 12: Effectivity indices of different estimators on the pore size study.

8.1.3 Pore shape

Pore shape is an important factor in determining structural behaviors in many aspects. In this benchmark, we simplify pore shape as an ellipse whose major and minor axis length are varied to study their influences on the accuracy of the proposed estimator. We use the same 2D cantilever beam as previous studies, but place two identical ellipse pores in the center and distanced by 1mm as in Figure 13. We fix the ellipse's major axis as 5 mm while varying its minor axis between 3.5 mm and 6.5 mm.

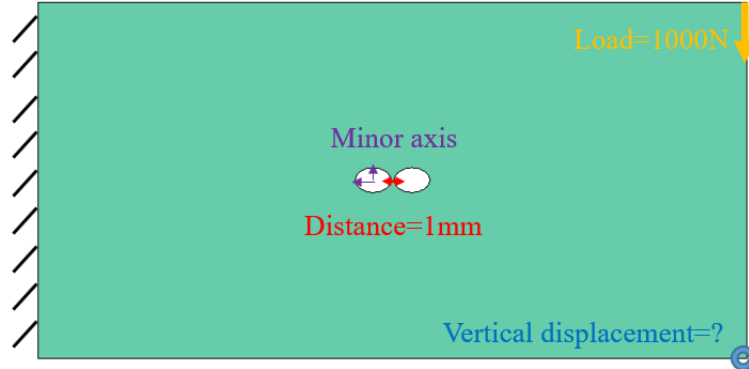


Figure 13: A 2D cantilever beam with boundary conditions and two pores with different aspect ratios.

If the quantity of interest is the vertical displacement at the right bottom corner, the comparisons between different estimators can be observed from Figure 14. For these two pores in proximity, it is observed the proposed second order estimator performs better than the other two. A plausible reason is due to strong interactions.

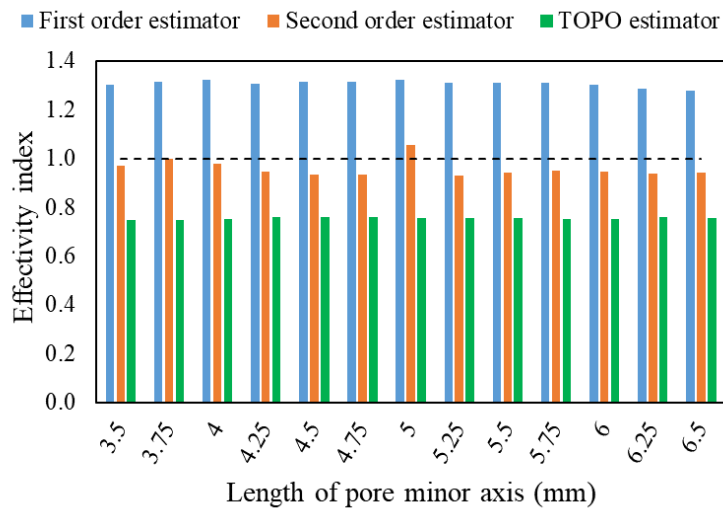


Figure 14: Effectivity indices of different estimators on the pore shape study.

8.1.4 Multiple pores

Manufactured metal components often contain many closely clustered pores, in which scenario the interaction range in complexity extends, from simple pair interactions to multiple pore interactions where the number of neighboring pores is gradually augmented. Therefore, in the last

benchmark example, we study the same beam but with multiple closely distanced pores in Figure 15.

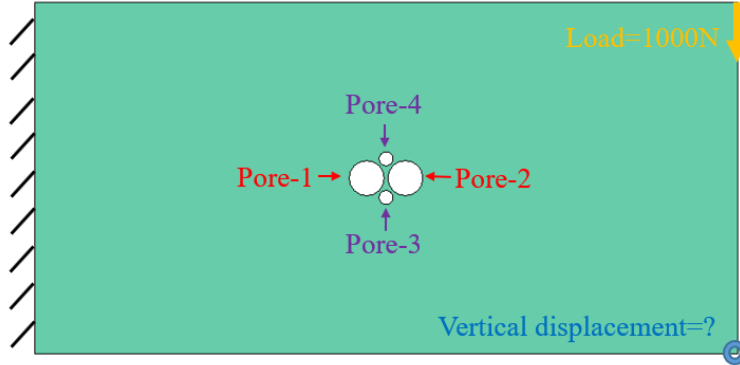


Figure 15: A 2D cantilever beam with boundary conditions and four pores with different sizes.

In Figure 15, four circular pores are symmetrically placed in the center of the beam such that the (surface-to-surface) distances between the two large pores (i.e., between pore-1 and pore-2) is 1.0 mm, and the distance between large and small pores (e.g., between pore-1 and pore-3) are 0.78 mm, and the distance between the two small pores (i.e., between pore-3 and pore-4) is 7.0 mm. Radii of pore-1 and pore-2 are 5 mm and radii of pore-3 and pore-4 are 2 mm. Similar to previous studies, the quantity of interest in this example is the vertical displacement at the bottom right corner of the beam.

The defeathering error of the pointwise displacement from the three estimators are compared with FEA results in Table 2. As one can see, the proposed second order estimator gives the best approximation due to its accountability for inter-pore interactions.

Table 2: Comparison of defeathering errors between different estimators.

FEA	D_{topo}	I_{topo}	D_{pore}^1	I_{pore}^1	D_{pore}^2	I_{pore}^2
6.21E-9	4.81E-9	1.29	4.82E-9	1.29	6.89E-9	0.91

To further illustrate the mechanism that the second order estimator is superior to the others, the three estimators are compared on each pore in Figure 16. There are two observations. First, by considering the difference between the first and second order estimators, it is obvious the interactions are significant in all pores. Second, by comparing the interaction with its first order estimator, it is obvious the interaction contributions are larger for small pores, which is consistent with the intuition that when a small pore interacts with a large one, the effect of the pairwise interaction is more significant on the small one compared to its first order estimator value.

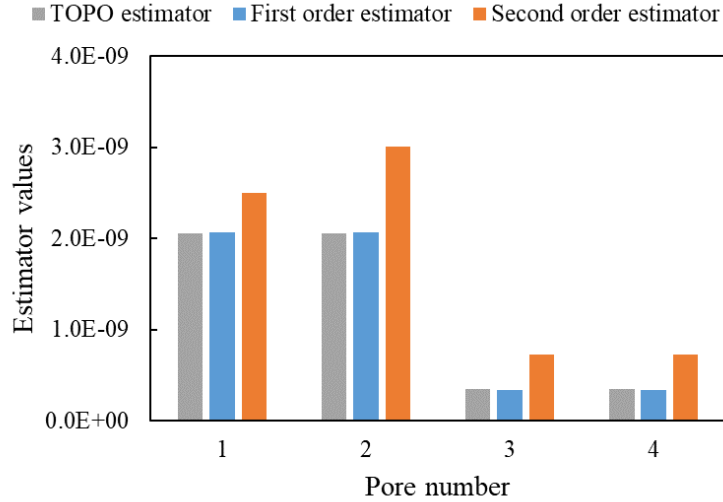


Figure 16: Comparison between different estimators on each pore for the model in Figure 15.

When multiple pores are clustered together, accounting for all interactions between different pairs can be nontrivial. For example, in this example which only has 4 pores, we have 6 pairwise interactions. In order to understand their relative importance, their values are compared in Figure 17. As can be noted, the interactions between two large pores, (i.e., between pore-1 and pore-2) are dominant, accounting for 63% of total interaction effects. Interactions between large and small pores (e.g., between pore-1 and pore-3) accounts for 6%-13%. On the other hand, the interactions between two small pores (i.e., between pore-3 and pore-4) appear trivial (about 0.07%) compared to others, which is due to their small sizes and long distances.

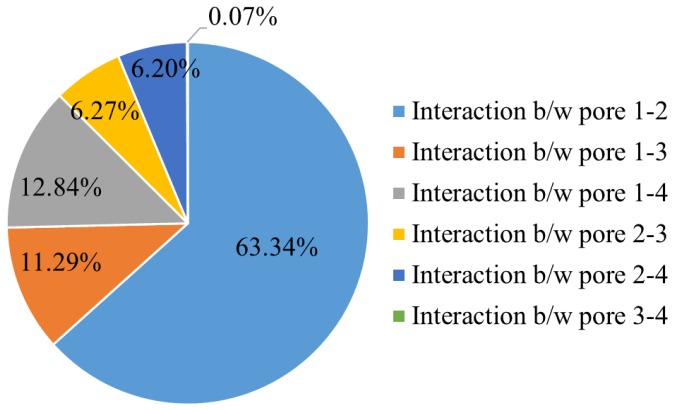


Figure 17: Comparisons between pairwise interactions for the 2D beam model.

Through the benchmark studies, we have demonstrated the proposed second order estimator is more robust and accurate than the others under the variations of pore distances, sizes, and shapes. In real applications, it is not rare many pores are clustered together in proximity. Under such scenario, it would be laborious to compute all pairwise interactions. Since it has been shown interactions between large pores in close distance seem to dominate among others, therefore, in the following case studies we only focus on the nearest-neighbor interactions between large pores.

The D_{topo} is also not listed for simplification. Please refer to [31] as for a detailed comparison between D_{topo} and D_{pore} .

8.2 Case study: 2D bracket

The first case is to study the impact of the presence of pores on a 2D bracket whose dimensions and boundary conditions are shown in Figure 18. While the bracket is constrained by the fixture hole on the right side, two vertical loads are applied from the top and bottom surfaces of the rectangular regions on the left side. The quantity of interest is the relative narrowing of the gap between the rectangular regions.

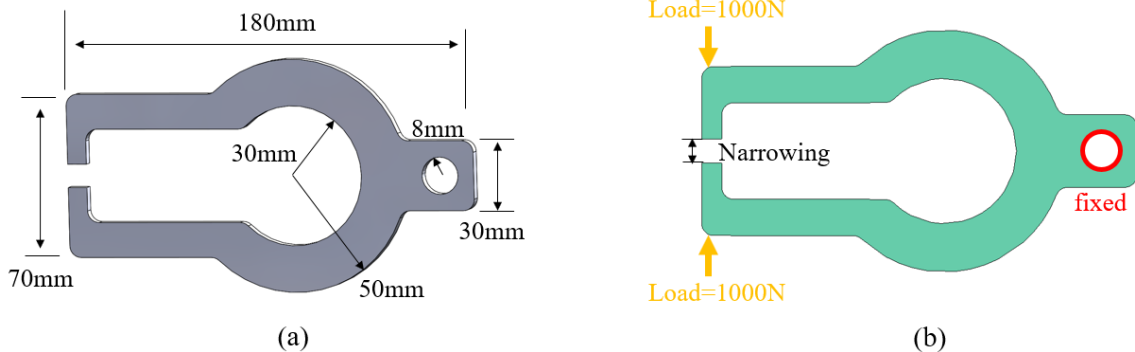


Figure 18: (a) The dimensions of the CAD model of the bracket; and (b) its 2D plane stress representation with prescribed boundary conditions.

We first study the relative narrowing as a function of the angular locations of two symmetrically located circular pores as shown in Figure 19. Both pores have the same diameters of 3mm.

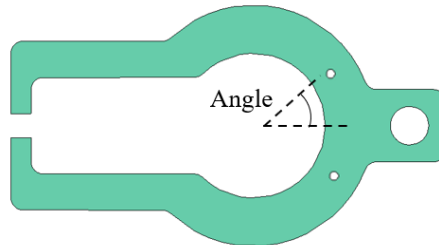


Figure 19: The 2D bracket with two symmetrically located circular pores.

When the angle is changed from 2.5 degrees to 120 degrees, the defeaturizing errors of the gap narrowing are summarized in Figure 20. The pore distance is dependent on their angular locations. For example, when the angle is 2.5 degrees, the distance is 3.8 mm and when the angle is 120 degrees, the distance is 70 mm. Thus, when the angle is small, the two pores are close to each other in which scenario the second order estimator is shown more closer to the FE ground truth. This is because the second order estimator considers pore-to-pore interaction effects. On the other hand, as the angle increases, the interaction between pores become weaker which results in similar results from both estimators.

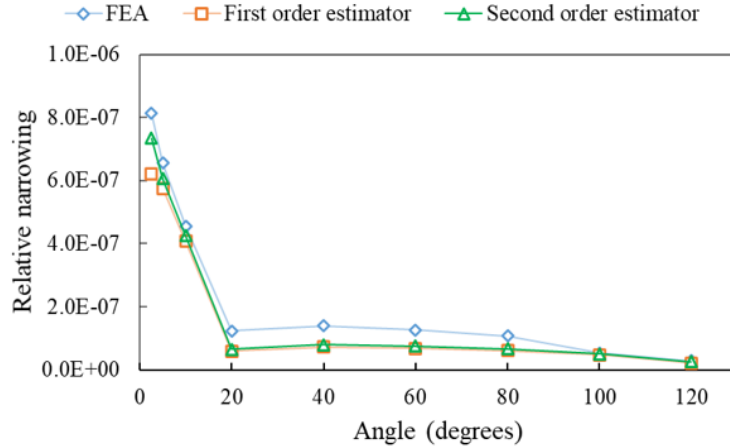


Figure 20: Relation between gap narrowing and pore angular locations for the 2D bracket model.

In order to test the proposed estimator in a scenario with manufacturing induced pores, we simulate the spatial distributions of potential pores via a casting simulation software, MAGMASOFT [49]. As shown in Figure 21(a), the simulation result indicates that casting pores would cluster in the central region between the fixture hole and its inner surface. To simulate the impacts of pore's actual morphologies, 6 pores of different morphologies, which are inspired by CT images from [17], are placed into this region as shown in Figure 21(b). Due to their relative positions, the pores are grouped with their nearest neighbors into three pairs. The average sizes and distances in each pair are summarized in Table 3. For the sake of simplification, pores are only assumed to interact with their nearest neighbors. Interactions between different pairs are neglected due to long distances.

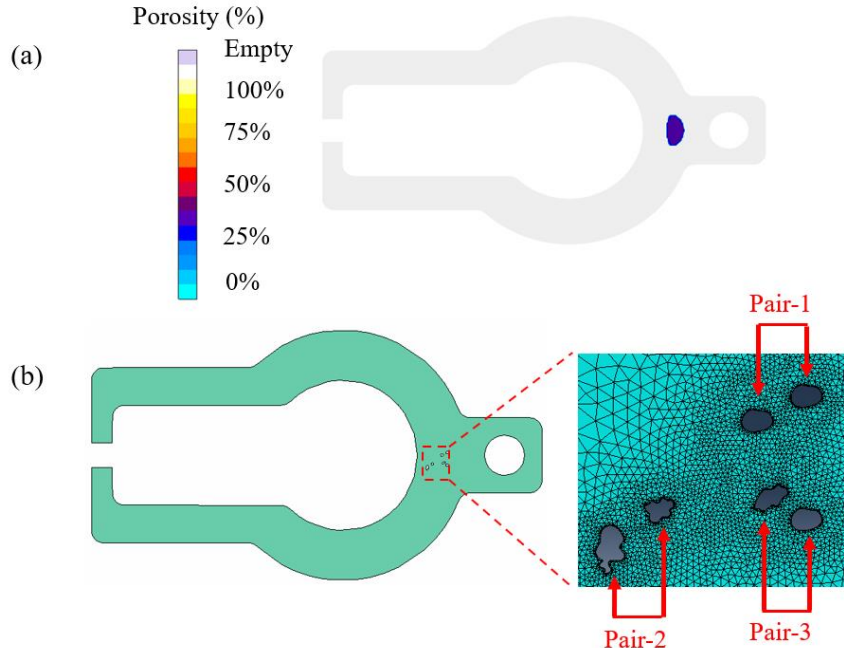


Figure 21: (a) Top view of the simulated pore distributions via MAGMASOFT; (b) the 2D bracket with multiple pore shapes from [17].

The defeathering error of the gap narrowing from FEA is 2.19e-7 mm, and the predictions from the first and second order estimators are 1.22e-7 mm and 1.87e-7 mm, respectively. It is therefore shown the second order estimator (with the effectivity index of 1.17) outperforms its first order counterpart (with the effectivity index of 1.79). To further compare the two estimators, their values in each pair are summarized in Table 3 where the sum of the fourth column (D_{pore}^1) equals to the total value of the first order estimation and the sum of the fifth columns (D_{pore}^2) equals the second order estimator. The percentages of the interaction effects in the seventh column range from 2.45% to 8.81% in different pairs. It should be noted that the percentage values are specific to each pair. The values are dependent on pore sizes, distances, shapes, and values of local field variables (e.g., displacement and stress). Comparing the percentage values between different pairs would be meaningless if they do not possess the same pore characteristics. Ideally, moving pores closer would generally increase their interactions in each pair.

Table 3: Parameters and estimator values for pores in the 2D bracket model.

	Average diameter (mm)	Distance (mm)	D_{pore}^1	D_{pore}^2	D_{int}^2	D_{int}^2/D_{pore}^2
Pair-1	1.00	2.24	1.39E-8	1.50E-8	6.30E-10	4.19%
Pair-2	1.28	2.50	9.01E-8	1.46E-7	1.29E-8	8.81%
Pair-3	1.10	1.81	1.81E-8	2.52E-8	6.17E-10	2.45%

8.3 Case study: 3D hook

In this case study, the proposed methodology is applied onto a 3D hook model whose overall dimensions and boundary conditions are illustrated in Figure 22(a). The model is subject to a vertical load inside the loading hole and the quantity of interest is a pointwise vertical displacement on the hook's shoulder section. In order to simulate porosity morphology in a more realistic way, a 3D synthetic pore model [13] is utilized in this section. This model, which is argued to have better pore presentations than ellipsoid and sphere shapes, is generated by intersecting three mutually perpendicular equivalent ellipsoids at their geometric centers as in Figure 22(b).

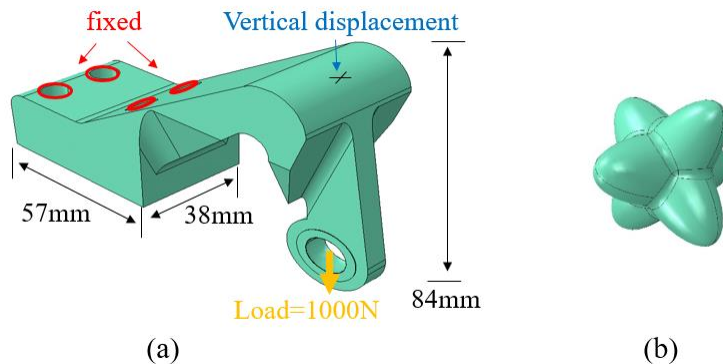


Figure 22: (a) CAD model of the 3D hook with boundary conditions and dimensions; and (b) 3D synthetic pore model [13].

15 synthetic models of different sizes are placed inside the hook model as shown in Figure 23. For each pore, its distance with every neighbor is computed and we assume only the nearest

neighbor is considered for pore interactions. Also, if the distance is more than five times of the pore sizes, we assume the interaction is too trivial to be considered. As a result, there are 10 out of the 15 pores, which have interactive neighbors, are labeled for interaction study as in Figure 23.

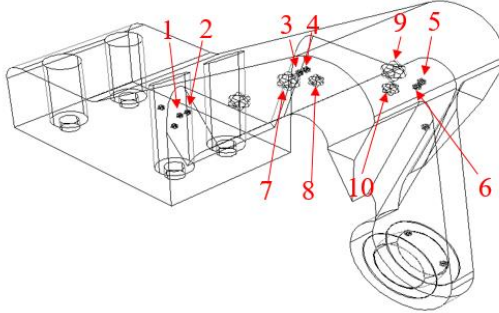


Figure 23: Spatial distribution of synthetic pores in the hook model where labeled pores are subject to pairwise interactions.

For the labeled pores in Figure 23, a summary of their sizes, interacting neighbors and inter-pore distances are provided in Table 4. It is noted from this table we only consider the one-to-one pore interactions for sake of simplification. For example, in the hook's neck region where pore-3, pore-4, pore-7 and pore-8 are located closely, we only consider the interactions in pair 3-4 and pair 7-8.

Table 4: Geometries and distances of pores in the 3D hook model.

Pore number	1	2	3	4	5	6	7	8	9	10
Interactive pore	2	1	4	3	6	5	8	7	10	9
Diameter (mm)	2.0	2.0	2.0	2.0	2.0	2.0	6.0	4.0	6.0	4.0
Distance (mm)	5.94	5.94	1.73	1.73	2.24	2.24	5.92	5.92	4.69	4.69

FEA results show the defeaturig error is 3.67E-8 mm for the presence of pores. The predictions from the first and second order estimators are 2.47e-8 mm and 3.14e-8 mm, respectively. It is clear it is the consideration of pore-to-pore interactions that makes the second order estimator more accurate.

Pairwise interactions are compared with each other, and their relative importance is shown in Figure 24. Several interesting observations can be drawn from this figure. First, the interaction between pore-7 and pore-8 is the dominant one, accounting for about 76.01% of the total interaction values. Specifically, comparing to the pair 9-10 which has identical pore sizes, similar inter-pore distance and accounts for 20.96%, the interaction in pair 7-8 is much stronger. One possible reason can be because the pair 7-8 locates in a region with higher stress values. Second, by comparing between pair 3-4 (about 1.7%) and 7-8, even though they are located in the same region, the interaction in the former pair is much smaller. This can be explained by their relatively small sizes. The same can be observed by comparison the pair 9-10 (about 20.96%) and 5-6 (about 1.25%). Lastly, the interaction in pair 1-2 is trivial (about 0.08%) compared with others due to their small sizes and large distance. It is therefore evident from this experiment, for parts with many pores, the most important pore-to-pore interactions comes from large neighboring pores in a highly stressed region.

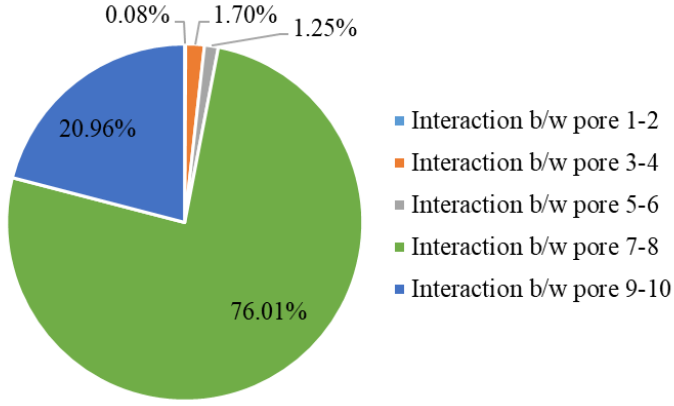


Figure 24: Comparison between pairwise pore interactions in the 3D bracket model.

8.4 Case study: 3D tensile bar

In the last case study, to test the performance of the proposed estimator on parts with actual manufacturing pores, we apply it to a manufactured tensile bar whose dimensions and loading conditions are described in Figure 25. To simulate a tension test, all degrees of freedom (DOF) on the top and bottom surfaces of gripping sections are fixed, and a uniform surface traction is applied as the tensile load as seen in Figure 25. The quantity of interest in this experiment is the pointwise displacement at a (yellow marked) point on the loading section.

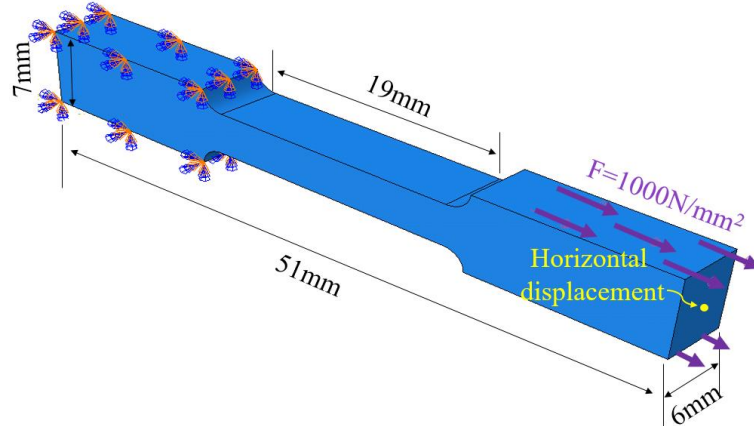


Figure 25: Dimensions and boundary conditions of the 3D tensile bar.

This tensile bar was scanned by a X-ray scanner, VALUCT [50] with $250 \mu\text{m}$ resolution. Porosity detection was performed based on the method of thresholding and segmentation between phase contrast in the Image Processing Toolbox in MATLAB [51]. The reconstructed pore geometry was then saved in a STL file whose mesh was then repaired in SALOME [52] to remove mesh defects, e.g., disconnected geometry, mis-oriented face, and intersected elements. After mesh clean-up, a surface mesh representation of the porous tensile bar is shown in Figure 26.

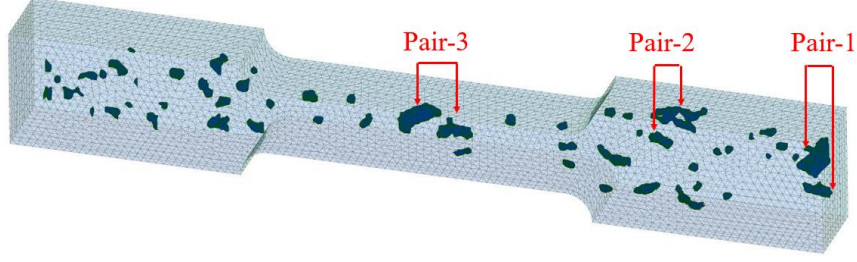


Figure 26: Surface representation of the tensile bar with tomography reconstructed pores where three pairs of pores are highlighted for interaction study.

It can be seen from Figure 26 that there are 58 internal pores whose equivalent radii range from 0.54 mm to 3.43mm. Among them, a gas pore (which is resulted from trapped gas or released hydrogen from solidified metal) tends to be spherical, while a shrinkage induced pore is more likely to be large and has irregular shape. While locations of pores generally indicate where the liquid metal is last to be solidified, it is noteworthy most pores in this tensile bar are distributed on the middle plane along the thickness direction. In the 58 pores, six pores (i.e., three pairs) are selected for interaction studies in this experiment. The reason for such selection comes from their relatively large sizes and the existence of their near neighbors. As recall from previous experiments, pore sizes and neighbor distance are two major factors in determining interaction magnitudes. The two factors on the selected pores are summarized in the first two columns of Table 5.

A volume mesh of 651,814 linear tetrahedral elements is generated from the surface mesh. Please note that the linear elements were automatically generated in the process of converting surface triangle mesh (STL) to tetrahedral volume mesh in ABAQUS. Higher order elements (if possible) are suggested for better stress computations. The volume mesh representation of the porous tensile bar is then solved by a direct FE whose result as a ground truth is compared with the proposed estimator. On the contrary, the porosity-oriented estimators only need to be computed on the reference model (no pores) in Figure 25. Since meshing the reference model only requires 87,747 linear tetrahedral elements, its mesh size is only about 13.5% of the direct FEA approach.

The defeaturizing error from FEA shows an incremental displacement of 3.54e-8 mm with the presence of pores. The predictions from the first and second order estimators are 1.63e-8 mm and 2.79e-8 mm, respectively. It is thus evident the higher order estimator is more accurate in this case. The values of the proposed estimators are detailed for each pair in Table 5. It should be noted the sum of the fourth column (D_{pore}^1) does not equal to the value of the first order estimation because this estimation also includes defeaturizing errors on other pores which are not studied in inter-pore interactions. The same applies to D_{pore}^2 . From this table, we can see pair-3 has higher estimations and interaction values than others, although they all have similar sizes and distances. One plausible reason is because pair-3 locates in the gauge section with reduced cross-sectional area and high stress concentrations (which contribute to higher values of estimators in Equation (7.1) and (7.2)). The percentages of interactions in estimators range from 1.95% to 3.62%. Stronger interactions would be expected if inter-pore distances are even smaller.

Table 5: Pore geometries and estimator values of the three pairs of pores in the 3D cantilever beam model.

	Average size (mm)	Distance (mm)	D_{pore}^1	D_{pore}^2	D_{int}^2	$D_{\text{int}}^2/D_{\text{pore}}^2$
Pair-1	3.13	2.47	4.67E-12	9.25E-12	3.35E-13	3.62%
Pair-2	2.97	1.75	8.01E-11	1.52E-10	2.42E-12	1.95%
Pair-3	3.18	2.89	7.04E-9	8.92E-9	2.01E-10	2.25%

The computational efficiency of the proposed method can be illustrated on this example in two perspectives. First, for any computational mesh dependent method, e.g., FEM, creation of a high-quality mesh is prerequisite. With the cost of central processing unit (CPU) time significantly decreasing, engineers usually spend most of their time in generating qualified mesh, which becomes a major bottleneck in a simulation project. In an ideal scenario, the project would be dramatically accelerated if the meshing process can be fully automated without human intervention [53]. However, if a high-fidelity simulation is demanded, automation of meshing is very difficult on complex geometries. For example, manufacturing pores often manifest complex morphologies with disconnected topologies, concave radii and sharp corners. Without human intervention, meshing singularity or even failure, e.g., inverted or tangled elements, is not rare [21]. Problematic mesh, if not taken care of, would result in ill-conditioned matrix in FE linear systems, which would further deteriorate computational accuracy and speed. Our proposed method only requires mesh on a dense domain, (i.e., simple geometry and no pores) where mesh automation is permitted and time for human intervention is saved. Second, in solving process, our method integrates the solutions from a defeatured FE with a boundary element approach. As in this example, the number of unknown variables of the defeatured FE (on dense geometry) only accounts for 13.5% of its direct FE counterpart, thus allowing a much smaller memory footprint and faster FE execution. Meanwhile, the speed of the boundary element method is also expected faster than a traditional FE with problem dimensions lowered by one [44]. With the two perspectives, we compare the time for both direct FE and the proposed method in Table 6.

Table 6: Time comparison (in seconds) on different steps between direct FEM and the proposed estimator.

	Direct FEM	Proposed
Pore reconstruction	19	19
Meshing	1210	2
Solving	243	101
Total time (sec)	1472	265

As seen from Table 6, the proposed method reduces the computational time of the direct FEM approach by 82%. In the meshing step, the major time cost of the direct method comes from human interventions to fix mesh singularities, e.g., mis-oriented faces, missing nodes, and ill-shaped volume elements due to the sharp corners on pore surfaces. In the solving process, solving direct FEM takes 243 seconds on the porous domain with the mesh size of 651,814. On the other hand, 55 seconds are for solving FE on the dense domain with mesh size of 87,747 and 46 seconds on boundary element method for solving exterior Neumann formulations for the first and second order estimators. It is noted the boundary element solver is executed in a non-optimized sequential manner in this work, which would further be accelerated by parallelization.

We have demonstrated this proposed method via several numerical experiments in this section. It is first tested on a benchmark example where the influences of various pore parameters are studied. It is then tested on different applications. In the bracket and hook models, pore spatial distributions are simulated by a casting software, and their shapes are represented by synthetic models. In the tensile bar model, the pores are created in a real casting process and their models are generated via tomography reconstructions. Through the benchmarks and applications, we have observed: (1) the proposed gradient-enhanced estimator, as a reliable and computational efficient alternative to direct FEA, is generally more accurate than its first order counterpart and the topological sensitivity based estimator; (2) pore-to-pore interactions are dependent on the ratio between inter-pore distances and pore sizes, while other important factors include pore shapes and values of local field variables; (3) for a metallic component containing many pores, interactions between closely distanced large ones in highly stressed regions are probably more critical than others, which often needs careful attentions. Although the approach is tested and verified by casting pores in the experiment section, its methodology is developed without a limitation to a specific manufacturing type. Thus, its extension to other manufacturing induced porosity problems (e.g., additive manufacturing) is possible but needs to be established.

9. CONCLUSIONS AND FUTURE WORKS

In this paper, a novel gradient-enhanced defeaturing method has been proposed to predict elastic structural behaviors with respect to manufacturing induced pores. The proposed method, which combines the merits from topological sensitivity, the first and second order shape sensitivities, is advantageous in accounting for various porosity morphological characteristics and pore-to-pore interactions. Its numerical advantage over direct FEA is that it only requires solutions from reference domains (without pores), thus avoiding mesh singularities and reducing computational costs.

There are several directions to expand the current work in future work. First, this method only predicts quantity of interests for linear elastic problems. It is well known both shape and topological sensitivities are well developed for nonlinear problems [23,24]. Extension of this work to analyze such problems is of great interest, e.g., fatigue analysis on porosity problem is arguably more important [11]. Second, material properties in this work are assumed to be isotropic. This assumption can be relaxed in future work to consider more realistic manufactured alloys with heterogeneous properties. Third, compared with pores in casting alloys, the pores in additive manufactured materials (e.g., titanium alloy) may have very different morphology and distribution due to different formation mechanisms [13]. Applying the proposed method to study additive manufacturing induced porosity problems has much value and its prediction accuracy needs to be investigated

ACKNOWLEDGEMENTS

The authors thank the ACRC consortium members for funding the project and also thank the industrial members of the focus group whose help was invaluable. Specifically, we appreciate Randy Beals from Magna International provided the W-profile plate samples for testing, and Chen Dai from VJ Technologies provided supports on X-ray computed tomography (CT) scanning and data generation.

APPENDIX

The volume formulation of the first order shape sensitivity for an arbitrary pointwise displacement field in Section 4.3 can be expressed as

$$\begin{aligned} \Psi'_{nd} = & \iiint_{\Omega} \left[\boldsymbol{\sigma}(\mathbf{z}) : \boldsymbol{\varepsilon}(\nabla \lambda^T \mathbf{V}) + \boldsymbol{\sigma}(\nabla \mathbf{z}^T \mathbf{V}) : \boldsymbol{\varepsilon}(\lambda) \right. \\ & \left. - \delta(\mathbf{x} - \hat{\mathbf{x}})^T (\nabla \lambda^T \mathbf{V}) - \delta(\mathbf{x} - \hat{\mathbf{x}})^T (\nabla \mathbf{z}^T \mathbf{V}) \right] d\Omega \\ & - \iint_{\Gamma} [\boldsymbol{\sigma}(\mathbf{z}) : \boldsymbol{\varepsilon}(\lambda)] V_n d\Gamma + \iint_{\Gamma^{f+s}} [\delta(\mathbf{x} - \hat{\mathbf{x}})^T \lambda] V_n d\Gamma \\ & + \iint_{\Gamma^s} \left\{ -\mathbf{f}^{sT} (\nabla \lambda^T \mathbf{V}) + [\nabla(\mathbf{f}^{sT} \lambda) \cdot \mathbf{n} + \Lambda(\mathbf{f}^{sT} \lambda)] V_n \right\} d\Gamma \end{aligned} \quad (\text{A.1})$$

The volume form of the second order shape sensitivity in Section 5.1 can be written as

$$\begin{aligned} & \langle D \langle D\psi; \mathbf{V} \rangle; \mathbf{W} \rangle \\ & = \iiint_{\Omega_{\eta}} \left[(\delta(\mathbf{x} - \hat{\mathbf{x}})^T \mathbf{z}) \nabla \mathbf{V} + \mathbf{M} \right] : \nabla \mathbf{W} d\Omega_{\eta} + \iiint_{\Omega_{\eta}} \left[\delta(\mathbf{x} - \hat{\mathbf{x}})^T \mathbf{z} + \mathbf{N} \right] \Theta d\Omega_{\eta} \end{aligned} \quad (\text{A.2})$$

in which

$$\begin{aligned} \mathbf{M} = & -[(\nabla \cdot \mathbf{V})(\nabla \lambda) \boldsymbol{\sigma}(\mathbf{z})] - [(\nabla \cdot \mathbf{V})(\nabla \mathbf{z}) \boldsymbol{\sigma}(\lambda)] \\ & - [((\nabla \lambda) \boldsymbol{\sigma}(\mathbf{z}) : \nabla \mathbf{V}) \mathbf{I}] - [((\nabla \mathbf{z}) \boldsymbol{\sigma}(\lambda) : \nabla \mathbf{V}) \mathbf{I}] \\ & + [\boldsymbol{\varepsilon}(\mathbf{P}) : \boldsymbol{\sigma}(\mathbf{z}) \mathbf{I}] - [\mathbf{P}^T \mathbf{f}^B \mathbf{I}] + [\boldsymbol{\varepsilon}(\lambda) : \boldsymbol{\sigma}(\mathbf{Q}) \mathbf{I}] \\ & + \frac{1}{2} \nabla \mathbf{z} \mathcal{C} (\nabla \mathbf{V}^T \nabla \lambda + \nabla \lambda^T \nabla \mathbf{V}) - \nabla \mathbf{P} \boldsymbol{\sigma}(\mathbf{z}) - \nabla \mathbf{z} \boldsymbol{\sigma}(\mathbf{P}) \\ & + \frac{1}{2} \nabla \lambda \mathcal{C} (\nabla \mathbf{V}^T \nabla \mathbf{z} + \nabla \mathbf{z}^T \nabla \mathbf{V}) - \nabla \lambda \boldsymbol{\sigma}(\mathbf{Q}) - \nabla \mathbf{Q} \boldsymbol{\sigma}(\lambda) \\ & + [\boldsymbol{\varepsilon}(\lambda) : \boldsymbol{\sigma}(\mathbf{z}) - \lambda^T \mathbf{f}^B - \nabla \lambda \boldsymbol{\sigma}(\mathbf{z}) - \nabla \mathbf{z} \boldsymbol{\sigma}(\lambda)] \nabla \mathbf{V} \end{aligned} \quad (\text{A.3})$$

where the term \mathbf{N} in Equation (A.2) does not need to be calculated because it will be dropped when transforming to a boundary form by Guillaume-Masmoudi lemma.

REFERENCES

- [1] J. Collot, “Review of New Process Technologies in the Aluminum Die-Casting Industry,” *Materials and Manufacturing Processes*, vol. 16, no. 5, pp. 595–617, Sep. 2001, doi: 10.1081/AMP-100108624.
- [2] C. Y. Yap *et al.*, “Review of selective laser melting: Materials and applications,” *Applied Physics Reviews*, vol. 2, no. 4, p. 041101, Dec. 2015, doi: 10.1063/1.4935926.
- [3] H. R. Ammar, A. M. Samuel, and F. H. Samuel, “Porosity and the fatigue behavior of hypoeutectic and hypereutectic aluminum–silicon casting alloys,” *International Journal of Fatigue*, vol. 30, no. 6, pp. 1024–1035, Jun. 2008, doi: 10.1016/j.ijfatigue.2007.08.012.
- [4] A. V. Catalina, S. Sen, D. M. Stefanescu, and W. F. Kaukler, “Interaction of porosity with a planar solid/liquid interface,” *Metall Mater Trans A*, vol. 35, no. 5, pp. 1525–1538, May 2004, doi: 10.1007/s11661-004-0260-z.
- [5] D. M. Stefanescu, *Science and Engineering of Casting Solidification*, 3rd Edition. Cham: Springer, 2015.
- [6] J. Stef *et al.*, “Mechanism of porosity formation and influence on mechanical properties in selective laser melting of Ti-6Al-4V parts,” *Materials & Design*, vol. 156, pp. 480–493, Oct. 2018, doi: 10.1016/j.matdes.2018.06.049.

[7] T. J. Jeon, T. W. Hwang, H. J. Yun, C. J. VanTyne, and Y. H. Moon, “Control of Porosity in Parts Produced by a Direct Laser Melting Process,” *Applied Sciences*, vol. 8, no. 12, Art. no. 12, Dec. 2018, doi: 10.3390/app8122573.

[8] M. Tang, P. C. Pistorius, and J. L. Beuth, “Prediction of lack-of-fusion porosity for powder bed fusion,” *Additive Manufacturing*, vol. 14, pp. 39–48, Mar. 2017, doi: 10.1016/j.addma.2016.12.001.

[9] H. Gong, K. Rafi, H. Gu, T. Starr, and B. Stucker, “Analysis of defect generation in Ti–6Al–4V parts made using powder bed fusion additive manufacturing processes,” *Additive Manufacturing*, vol. 1–4, pp. 87–98, Oct. 2014, doi: 10.1016/j.addma.2014.08.002.

[10] A. M. Waters, “Three-dimensional analysis of voids in AM60B magnesium tensile bars using computed tomography imagery. PhD thesis,” Johns Hopkins University, 2001.

[11] V. Prithivirajan and M. D. Sangid, “The role of defects and critical pore size analysis in the fatigue response of additively manufactured IN718 via crystal plasticity,” *Materials & Design*, vol. 150, pp. 139–153, Jul. 2018, doi: 10.1016/j.matdes.2018.04.022.

[12] S. Ghosh, K. Lee, and P. Raghavan, “A multi-level computational model for multi-scale damage analysis in composite and porous materials,” *International Journal of Solids and Structures*, vol. 38, no. 14, pp. 2335–2385, Apr. 2001, doi: 10.1016/S0020-7683(00)00167-0.

[13] T. Taxer, C. Schwarz, W. Smarsly, and E. Werner, “A finite element approach to study the influence of cast pores on the mechanical properties of the Ni-base alloy MAR-M247,” *Materials Science and Engineering: A*, vol. 575, pp. 144–151, Jul. 2013, doi: 10.1016/j.msea.2013.02.067.

[14] L. Xia and P. Breitkopf, “Recent Advances on Topology Optimization of Multiscale Nonlinear Structures,” *Arch Computat Methods Eng*, vol. 24, no. 2, pp. 227–249, Apr. 2017, doi: 10.1007/s11831-016-9170-7.

[15] S. Leuders *et al.*, “On the mechanical behaviour of titanium alloy TiAl6V4 manufactured by selective laser melting: Fatigue resistance and crack growth performance,” *International Journal of Fatigue*, vol. 48, pp. 300–307, Mar. 2013, doi: 10.1016/j.ijfatigue.2012.11.011.

[16] G. Kasperovich, J. Haubrich, J. Gussone, and G. Requena, “Correlation between porosity and processing parameters in TiAl6V4 produced by selective laser melting,” *Materials & Design*, vol. 105, pp. 160–170, Sep. 2016, doi: 10.1016/j.matdes.2016.05.070.

[17] P. Baicchi, G. Nicoletto, and E. Riva, *Modeling the influence of pores on fatigue crack initiation in a cast Al-Si alloy*. CP2006, 2006.

[18] M. Ries, C. Krempaszky, B. Hadler, and E. Werner, “The influence of porosity on the elastoplastic behavior of high performance cast alloys,” *PAMM*, vol. 7, no. 1, pp. 2150005–2150006, Dec. 2007, doi: 10.1002/pamm.200700159.

[19] Z. Shan and A. M. Gokhale, “Micromechanics of complex three-dimensional microstructures,” *Acta Materialia*, vol. 49, no. 11, pp. 2001–2015, Jun. 2001, doi: 10.1016/S1359-6454(01)00093-3.

[20] Y. Hangai and S. Kitahara, “Quantitative Evaluation of Porosity in Aluminum Die Castings by Fractal Analysis of Perimeter,” *Materials Transactions*, vol. 49, no. 4, pp. 782–786, 2008, doi: 10.2320/matertrans.MRA2007314.

[21] J. Danczyk and K. Suresh, “Finite element analysis over tangled simplicial meshes: Theory and implementation,” *Finite Elements in Analysis and Design*, vol. 70–71, pp. 57–67, Aug. 2013, doi: 10.1016/j.finel.2013.04.004.

[22] R. D. Cook, *Concepts and applications of finite element analysis*. John wiley & sons, 2007.

[23] K. K. Choi and N.-H. Kim, *Structural Sensitivity Analysis and Optimization 1: Linear Systems*. Springer Science & Business Media, 2006.

[24] M. P. Bendsoe and O. Sigmund, *Topology Optimization: Theory, Methods, and Applications*. Springer Science & Business Media, 2013.

[25] M. Li and S. Gao, “Estimating defeathering-induced engineering analysis errors for arbitrary 3D features,” *Computer-Aided Design*, vol. 43, no. 12, pp. 1587–1597, Dec. 2011, doi: 10.1016/j.cad.2011.08.006.

[26] M. Li, B. Zhang, and R. R. Martin, “Second-order defeathering error estimation for multiple boundary features,” *International Journal for Numerical Methods in Engineering*, vol. 100, no. 5, pp. 321–346, 2014, doi: 10.1002/nme.4725.

[27] S. H. Gopalakrishnan and K. Suresh, “A formal theory for estimating defeathering-induced engineering analysis errors,” *Computer-Aided Design*, vol. 39, no. 1, pp. 60–68, Jan. 2007, doi: 10.1016/j.cad.2006.09.006.

[28] I. Turevsky, S. H. Gopalakrishnan, and K. Suresh, “Defeathering: A posteriori error analysis via feature sensitivity,” *International Journal for Numerical Methods in Engineering*, vol. 76, no. 9, pp. 1379–1401, 2008, doi: 10.1002/nme.2345.

[29] S. Deng, C. Soderhjelm, D. Apelian, and K. Suresh, “Estimation of elastic behaviors of metal components containing process induced porosity,” *Computers & Structures*, vol. 254, p. 106558, Oct. 2021, doi: 10.1016/j.compstruc.2021.106558.

[30] C.-J. Chen and K. K. Choi, “A continuum approach for second-order shape design sensitivity of elastic solids with loaded boundaries,” *International Journal for Numerical Methods in Engineering*, vol. 38, no. 17, pp. 2979–3004, 1995, doi: 10.1002/nme.1620381708.

[31] S. Deng, C. Soderhjelma, D. Apelian, and K. Suresh, “Estimation of Elastic Behaviors for Metal Castings with Manufacturing Induced Porosities,” *in review*, 2020.

[32] A. A. Novotny, R. A. Feijóo, E. Taroco, and C. Padra, “Topological sensitivity analysis for three-dimensional linear elasticity problem,” *Computer Methods in Applied Mechanics and Engineering*, vol. 196, no. 41, pp. 4354–4364, Sep. 2007, doi: 10.1016/j.cma.2007.05.006.

[33] J. Sokolowski and A. Zochowski, “On the Topological Derivative in Shape Optimization,” *SIAM J. Control Optim.*, vol. 37, no. 4, pp. 1251–1272, Jan. 1999, doi: 10.1137/S0363012997323230.

[34] H. A. Eschenauer, V. V. Kobelev, and A. Schumacher, “Bubble method for topology and shape optimization of structures,” *Structural Optimization*, vol. 8, no. 1, pp. 42–51, Aug. 1994, doi: 10.1007/BF01742933.

[35] A. A. Novotny, R. A. Feijóo, E. Taroco, and C. Padra, “Topological-Shape Sensitivity Method: Theory and Applications,” in *IUTAM Symposium on Topological Design Optimization of Structures, Machines and Materials*, Dordrecht, 2006, pp. 469–478. doi: 10.1007/1-4020-4752-5_45.

[36] S. Deng and K. Suresh, “Multi-constrained topology optimization via the topological sensitivity,” *Struct Multidisc Optim*, vol. 51, no. 5, pp. 987–1001, May 2015, doi: 10.1007/s00158-014-1188-6.

[37] S. Deng and K. Suresh, “Multi-constrained 3D topology optimization via augmented topological level-set,” *Computers & Structures*, vol. 170, pp. 1–12, Jul. 2016, doi: 10.1016/j.compstruc.2016.02.009.

[38] S. Deng and K. Suresh, “Topology optimization under thermo-elastic buckling,” *Struct Multidisc Optim*, vol. 55, no. 5, pp. 1759–1772, May 2017, doi: 10.1007/s00158-016-1611-2.

[39] S. Deng and K. Suresh, “Stress constrained thermo-elastic topology optimization with varying temperature fields via augmented topological sensitivity based level-set,” *Struct Multidisc Optim*, vol. 56, no. 6, pp. 1413–1427, Dec. 2017, doi: 10.1007/s00158-017-1732-2.

[40] D. A. Tortorelli and W. Zixian, “A systematic approach to shape sensitivity analysis,” *International Journal of Solids and Structures*, vol. 30, no. 9, pp. 1181–1212, Jan. 1993, doi: 10.1016/0020-7683(93)90012-V.

[41] W. Kecs and P. Teodorescu, *Applications of the theory of distributions in mechanics*. Taylor & Francis, 1974.

[42] E. Taroco, G. C. Buscaglia, and R. A. Feljóo, “Second-order shape sensitivity analysis for nonlinear problems,” *Structural Optimization*, vol. 15, no. 2, pp. 101–113, Apr. 1998, doi: 10.1007/BF01278496.

[43] S. Boyd and L. Vandenberghe, *Convex Optimization*, 1st Edition. Cambridge, UK ; New York: Cambridge University Press, 2004.

[44] A. A. Becker, *The boundary element method in engineering: a complete course*. McGraw-Hill Companies, 1992.

[45] Y. J. Liu, “A fast multipole boundary element method for 2D multi-domain elastostatic problems based on a dual BIE formulation,” *Comput Mech*, vol. 42, no. 5, pp. 761–773, Oct. 2008, doi: 10.1007/s00466-008-0274-2.

[46] P. Bettess, “Infinite elements,” *International Journal for Numerical Methods in Engineering*, vol. 11, no. 1, pp. 53–64, 1977, doi: 10.1002/nme.1620110107.

[47] “ABAQUS/Standard User’s Manual, Version 6.9. / Smith, Michael. Providence, RI : Dassault Systèmes Simulia Corp, 2009.”

[48] S. Prudhomme, J. T. Oden, T. Westermann, J. Bass, and M. E. Botkin, “Practical methods for a posteriori error estimation in engineering applications,” *International Journal for Numerical Methods in Engineering*, vol. 56, no. 8, pp. 1193–1224, 2003, doi: 10.1002/nme.609.

[49] “Magmasoft-5.1-Tutorial,” *Software training, tutorials, download, torrent*, Dec. 15, 2011. <http://www.crackcad.com/magmasoft-5-1-tutorial/> (accessed Sep. 16, 2020).

[50] “ValuCT – VJ Technologies.” <https://vjt.com/valuct-system/> (accessed Sep. 29, 2020).

[51] “MATLAB. (2010). version 7.10.0 (R2010a). Natick, Massachusetts: The MathWorks Inc.”

[52] A. Ribes and C. Caremoli, “Salomé platform component model for numerical simulation,” in *31st Annual International Computer Software and Applications Conference (COMPSAC 2007)*, Jul. 2007, vol. 2, pp. 553–564. doi: 10.1109/COMPSAC.2007.185.

[53] G. R. Liu, *Mesh Free Methods: Moving Beyond the Finite Element Method*, 1st edition. CRC Press, 2002.